Title:

Spatial and molecular anatomy of germ layers in the gastrulating Cynomolgus monkey embryo

Guizhong Cui[1,8], Su Feng[1,8], Yaping Yan[2,8], Li Wang[3], Xiechao He[4], Xi Li[2], Yanchao Duan[2], Jun Chen[5], Patrick P.L. Tam[6], Ke Tang[7], Ping Zheng[4], Wei Si[2,*], Naihe Jing[1,3,*], Guangdun Peng[1,3,9,*]

[1]Bioland Laboratory (Guangzhou Regenerative Medicine and Health Guangdong Laboratory), Guangzhou 510005, China

[2]Yunnan Key Laboratory of Primate Biomedical Research, Institute of Primate Translational Medicine, Kunming University of Science and Technology, Kunming, Yunnan, 650500, China

[3]Ceter for Cell Lineage and Development, CAS Key Laboratory of Regenerative Biology, Guangdong Provincial Key Laboratory of Stem Cell and Regenerative Medicine, Guangzhou Institutes of Biomedicine and Health, Chinese Academy of Sciences, University of Chinese Academy of Sciences, Guangzhou 510530, China

[4]State Key Laboratory of Genetic Resources and Evolution and Yunnan Key Laboratory of Animal Reproduction, Kunming Institute of Zoology, Chinese Academy of Sciences, Kunming 650223, China

[5]Department of Endocrinology, Qilu Hospital, Cheeloo College of Medicine, Shandong University, Jinan 250012, China

[6]Embryology Research Unit, Children's Medical Research Institute, School of Medical Sciences, Faculty of Medicine and Health, University of Sydney, Westmead, New South Wales, Australia

[7]Precise Genome Engineering Center, School of Life Sciences, Guangzhou University, Guangzhou, Guangdong 510006, China

[8]These authors contributed equally

[9]Lead contact

*Correspondence: siw@lpbr.cn (W.S.), jing_naihe@grmh-gdl.cn (N.J.), peng_guangdun@gibh.ac.cn (G.P.)

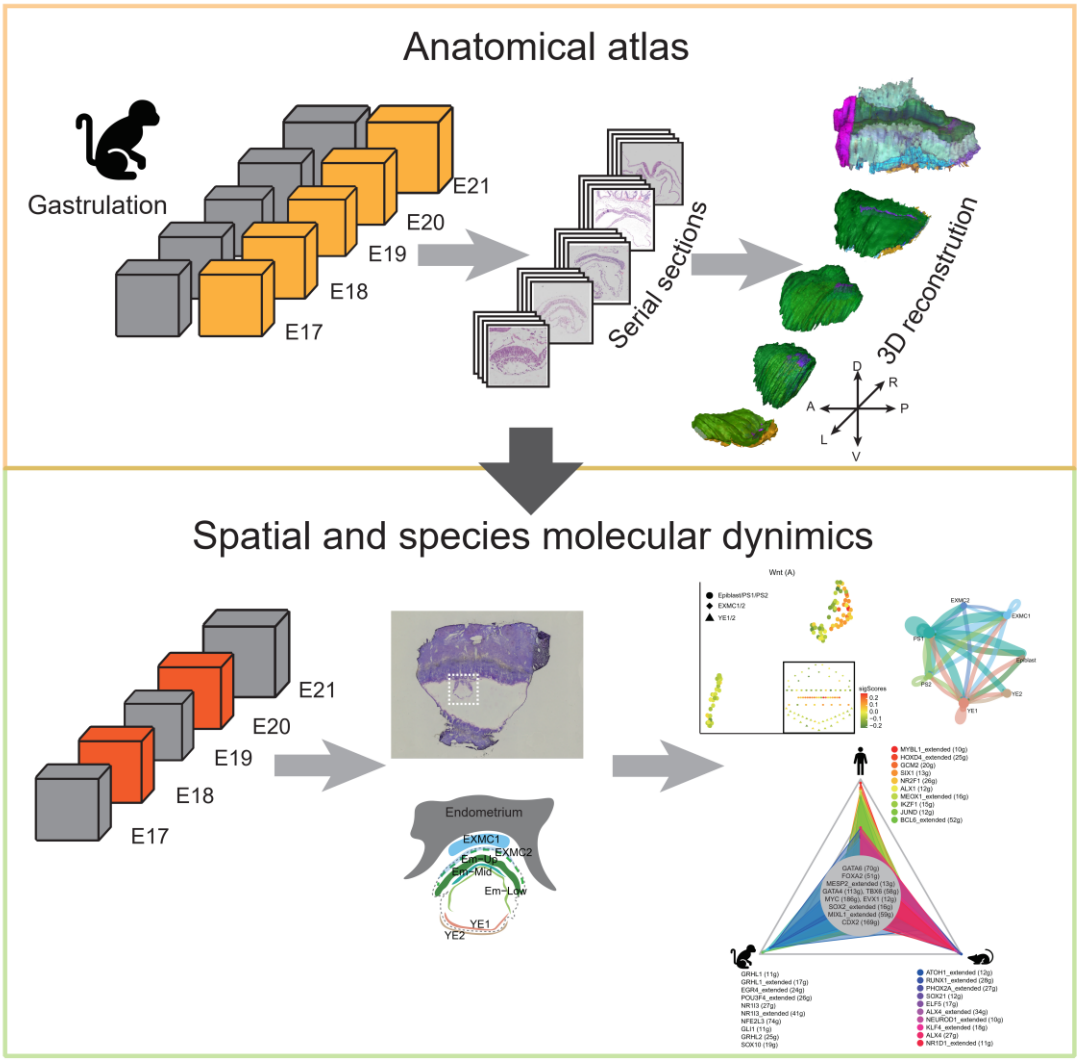

Highlight:

- A high-resolution anatomical atlas of Cynomolgus gastrulation embryos
- Created a three-dimensional digital template from serial sections of five developmental stages
- A two-dimensional spatiotemporal transcriptome of the germ layers of gastrulating embryos
- Cross-species comparison infers conservation of functional attributes of regulome and signaling activity in germ layer formation

Summary:

During mammalian embryogenesis, spatial regulation of gene expression and cell signaling are functionally coupled with lineage specification, patterning of tissue progenitors and germ layer morphogenesis. While the mouse model has been instrumental for our understanding of mammalian development, comparatively little is known about human and non-human primate gastrulation due to the restriction of both technical and ethical issues. Here, we present a morphological and molecular survey of spatiotemporal dynamics of cell types populating the non-human primate embryos during gastrulation. We performed serial sections of Cynomolgus monkeys (*Macaca fascicularis*) gastrulating embryos at 1-day temporal resolution from E17 to E21, and reconstructed three-dimensional digital models based on high-resolution anatomical atlas that revealed the dynamic changes in the geography of the mesoderm and primitive streaks. Spatial transcriptomics identified unique gene profiles that correspond to distinct germ layers and cross-species spatiotemporal transcriptome analysis revealed a developmental coordinate of germ layer segregation between mouse and primate. Furthermore, we identified species-specific transcription programs during gastrulation. These results offer important insights into evolutionarily conserved and divergent processes during mammalian gastrulation.

Key words

Germ layers, Gastrulation, Monkey embryo, Tissue lineages, Morphology, Spatial transcriptome, Cross-species analysis

68 # Introduction

69 Gastrulation is fundamental for mammalian embryogenesis at which the
70 definitive germ layers are established and the embryonic cell lineages are
71 allocated to the basic body plan. During germ layer formation, cells undergo
72 ordered changes in shape and fate under a spatiotemporally coordinated
73 regulation. The anatomy of gastrulation has been studied in a variety of
74 mammal species, including the mouse, human and nonhuman primate (Enders
75 et al., 1986; Grobstein, 1985; Mittnenzweig et al., 2021; Moore et al., 1985;
76 Nakamura et al., 2016; Pfister et al., 2007; Snow, 1977; Tarara et al., 1987;
77 Tyser et al., 2020; Yang et al., 2021). In human embryos, the embryonic period
78 is divided into 23 distinct morphological stages known as Carnegie stages (CS)
79 (O'Rahilly and Muller, 2010). At the early CS6 stage (approximately 14 days
80 post-fertilization, Embryonic day 14, E14), the posterior side of the pluripotent
81 epiblast cells start gastrulating to generate three germ layer cells: the ectoderm,
82 mesoderm, and endoderm. However, due to the limitation of the scope of
83 experimental studies of human development up to the onset of gastrulation
84 (Hyun et al., 2021) and the accessibility of embryonic samples, the
85 developmental biology of the gastrulating human embryos is not known in detail.
86

87 Previous works have described the gastrulation of non-human primates in the
88 context of morphogenesis and transcriptome, based on a few tissue sections
89 and in vitro models (Hendrickx, 1972; Luckett, 1978; Ma et al., 2019; Nakamura
90 et al., 2016; Niu et al., 2019; Tyser et al., 2020; Yang et al., 2021). However,
91 little is known about the three-dimensional (3D) structure and the molecular
92 landscape, such as the spatiotemporal pattern of gene expression, of
93 gastrulating embryos, both of which are crucial for gaining structural insights of
94 physiology and illustrating fate mapping. Importantly, in light of the kindled

interest of in vitro development of human and monkey early post-implantation embryo and the stem-cell based embryo models (Fu et al., 2020; Moris et al., 2020; Niu et al., 2019; Xiang et al., 2019; Zheng et al., 2019), it is imperative to gain the knowledge of in vivo benchmarks of post-implantation development particularly at gastrulation for use as a reference framework for interpreting the outcome of in vitro modeling research. Therefore, high-resolution morphological and spatial transcriptomic analysis of macaque gastrulating embryos is an imperative scientific endeavour.

With the advent of single-cell RNA sequencing, the molecular phenotype of cell types and their developmental trajectory in early mammalian development have been unraveled (Nakamura et al., 2016; Peng et al., 2020b; Pijuan-Sala et al., 2018; Tam and Ho, 2020; Tyser et al., 2020). However, the datasets of single-cell molecular signatures are missing the spatial/positional information of the cells of interest in embryo (Larsson et al., 2021; Peng et al., 2020a). Our previous work showed that spatially resolved transcriptome, not only generates a 3D digital “in situ hybridization” gene expression dataset for mouse gastrulation, also enables the reconstruction of the molecular trajectory of cell populations at gastrulation in time and space (Peng et al., 2019). As the morphogenetic program of immediate post-implantation development of the embryo is different between the mouse and the human, it is far from certain that the rodent-specific developmental mechanism can be extrapolated to the human embryo. It is a widely held view that non-human primate is the more appropriate model for human embryo development (Nakamura et al., 2021). However, systematic profiling of spatial transcriptome in gastrulating monkey embryos has yet to be accomplished, albeit single-cell transcriptome has been documented for Cynomolgus monkey embryo at E6- E17, which did not extend to the gastrulation stages. Here we performed Geo-seq (Chen et al., 2017) to

interrogate the molecular architecture and lineage commitment of the Cynomolgus monkey gastrulation embryos. We first established a high-resolution anatomical atlas to describe the key morphogenetic processes and three-dimensional topographical change during three germ layers formation of Cynomolgus monkey embryo. We then established a molecular atlas depicting the spatial pattern of gene expression at two timepoints (E18 and E20) of gastrulation. Finally, we undertook cross-species comparative analysis of spatiotemporal transcriptome data of mouse, Cynomolgus monkey and human embryos to identify molecular programs that may underpin the evolutional convergence, as well as divergence, of the developmental mechanism of gastrulation across these species. Our atlas can be explored via the interactive website: http://113.105.131.191:10010/Primate.Gastrulation/.

Results

Structural characteristics of gastrulating embryos in non-human primate

Cynomolgus monkey (*Macaca fascicularis*) gastrulating embryos (E17, E18, E19, E20 and E21, equivalent of carnegie stage 6-9) were isolated after in vitro fertilization (IVF) procedure with ethical approval (STAR Methods, Figure 1A-E and S1A-C). The embryos were staged by calculating the gestation days aided by transabdominal ultrasound monitoring. At least two embryo replicates at each developmental stage were studied (Figure S1C) with a very good consistence (Figure 1A-D, S1D-E and Figure S7G). Having the complete representation of embryos of gastrulation stages allow us to build a holistic view of tissue morphogenesis for non-human primates.

148

149 Corroborating previous observations on human and rhesus embryos (Enders
150 et al., 1986; Ghimire et al., 2021; Grobstein, 1985; Luckett, 1978; Nakamura et
151 al., 2016), post-implantation Cynomolgus embryos acquired a disc-like
152 configuration and are located on the center of the dome-shaped implantation
153 site which protrudes above the endometrial surface (Figure 1A-E). The
154 extraembryonic mesenchyme has invaded the primary villi to form the
155 secondary villi at E17 (Figure 1A and A', black arrow). At the tips of secondary
156 villi, cytotrophoblast (CT) cell converged into a thick cytotrophoblastic sheath
157 interspersed with syncytiotrophoblast (ST). Rodent extraembryonic mesoderm
158 originates from the epiblast during gastrulation, whereas the developmental
159 origin of primate extraembryonic mesoderm is hypothesized mainly from the
160 hypoblast-derived primary yolk sac (Bianchi et al., 1993; Ross and Boroviak,
161 2020). Remarkably, we found that in contrast to mouse, extraembryonic
162 mesoderm of primate embryos was formed before the onset of gastrulation
163 (Figure 1A'). As previously reported, the primate extraembryonic mesoderm
164 constituted the tissues that support the epithelium of the amnion and yolk sac
165 and the chorionic villi (Figure 1A'-E') (Carlson, 2015). Additionally, the
166 extraembryonic mesoderm splits into two layers, extraembryonic somatic
167 mesoderm (EXSOM) lining the amnion and extraembryonic splanchnic
168 mesoderm (EXSPM) lining the yolk sac (Figure 1A'-E'). These extraembryonic
169 mesoderm cells were subsequently merged with primitive streak (PS)-derived
170 extraembryonic mesoderm to establish the connecting stalk (embryonic stalk),
171 which attaches the whole conceptus to the chorion (Figure 1A' and Figure S2-
172 6)(Enders and King, 1988). Of note, a unique feature of primate embryos is the
173 formation of secondary yolk sac (SYS) on the hypoblast side the embryonic
174 disc (ED), consisted of an expanding hypoblast (HYP) and squamous yolk sac
175 parietal endoderm (YSPE), gradually expand following gastrulating (Figure 1A'-

176 E'). In the opposite side of ED, amniotic cavity (AC), consisting of a fluid-filled
177 sac surrounding the embryo, was enclosed by low cuboidal epithelium shaped
178 amnion (AM) with epiblast cells.
179
180 The formation of the primitive streak (PS) in the midline of the embryonic disc
181 heralds the onset of gastrulation. The epiblast (EPI) was pseudostratified with
182 the properties of typical epithelial cells, and with the elongation of the PS,
183 epiblast cells undergo epithelial-to-mesenchymal transition (EMT) to ingress
184 toward the space between the epiblast and hypoblast, generating mesoderm
185 (ME) wings (Figure 1A'-D'). The anterior-posterior length of epiblast increases
186 from 200μm at early gastrulation (E17) to 900μm at late gastrulation (E20)
187 (Figure 1F and Table S1). The primitive streak spans 20% of the anterior-
188 posterior length of the embryonic disc at E17, increasing to 40% by E20 (Figure
189 S1J). The PS gradually extends to the anterior epiblast, marking a progress of
190 gastrulation (Ghimire et al., 2021; Muller and O'Rahilly, 2004).
191

192 Cell number and cell cycle kinetics of primate gastrulating 193 embryos

194 A remarkable feature of the development of gastrulating embryos is the
195 regulation of cell growth, especially the mitotic division that results in the
196 increase in cell numbers. In mouse, the embryo that lack normal numbers of
197 cells due to the disruption of cell proliferation or cell death will delay gastrulation
198 until the appropriate number of epiblast cells has been attained (Snow, 1977;
199 Tam and Behringer, 1997). However, the number of cells of the primate embryo
200 during gastrulation remains to be investigated. We obtained a near complete
201 collection of tissue sections, therefore we applied detailed histological analyses
202 on serial sections to determine the kinetics of cell division (STAR Methods,

203 Figure 1G and S1F-I, Table S2). At E17, the early stage of primate gastrulation,
204 the epiblast was about 850 cells, and the hypoblast was approximately 370 cells
205 (Figure 1G and S1K). Subsequently, the number of cells in gastrulating
206 embryos increased rapidly. By the end of gastrulation, the whole embryo was
207 about 9100 cells (4500 cells in the ectoderm, 2200 cells in the mesoderm, and
208 2300 cells in the endoderm) (Figure 1G and S1K). Analysis of growth rate by
209 determining cell number increase, and by mapping mitotic activity in the germ
210 layers showed that the cell generation time for epithelial ectoderm and
211 endoderm was estimated at about 27 hours (Figure S1K). Notably, the average
212 cell generation time of the mesoderm, perhaps caused by the migration of
213 epiblast and the proliferation of nascent mesoderm, was significantly shortened
214 to 16 hours (Figure S1K). Given that the primitive streak covered about 1/5 of
215 the epiblast at E17 (Figure S1J), the initiation of gastrulation in Cynomolgus
216 monkey embryo was estimated to be approximately at E16 (Nakamura et al.,
217 2021; Nakamura et al., 2016). To assess the threshold number of epiblast cells
218 which is critical for the initiation of gastrulation, the epiblast and hypoblast at
219 starting gastrulation were calculated about 490 and 200 cells, respectively,
220 based on the kinetics of cell proliferation in macaque embryo. Interestingly, the
221 mean cell generation time during primate gastrulation was the half of pre-
222 gastrulation, which is consistent with the pattern found in mouse (Figure S1L)
223 (Snow, 1977). In addition, the length of epiblast progressively increases and the
224 size of the embryo becomes larger (Figure 1F, Table S1). That is slightly
225 different from the in vitro culture system (Niu et al., 2019). Both in vivo and in
226 vitro embryos have similar same size at the early stage of gastrulation, but
227 subsequently, natural embryos become larger while cultured embryos do not
228 change too much in size. This discrepancy may be due to the limitation of the
229 in vitro culture system for complex structural development.
230

Cellular anatomy of primate gastrulation embryo

Morphogenetic movements including cell migration and reorganization during gastrulation reshape the embryos. A paramount event is the epithelial to mesenchymal transition (EMT). EMT involves changes of epiblast cells from a proper epithelium with the full array of epithelial characteristics to mesenchymal-shaped mesoderm cells (Massri et al., 2021). During the initiation of mouse gastrulation, the PS, a transient embryonic structure where gastrulation EMT took place, was formed at the posterior of the epiblast. We observed that EMT follows similar patterns in monkey embryos (Figure 2 G-H and G'-H', white open arrowheads). The epiblast cells were contiguous with amnion cells at the margin of the disc, where there was a gradation in cell size from columnar to low cuboidal spanning two to three cells (Figure 2 E-F and E'-F', asterisks). Cells that remain in the epiblast are allocated to the ectoderm (ECT) (Ghimire et al., 2021; Shahbazi, 2020). A thick basement membrane lining the epiblast surface was visible in the anterior region (Figure 2 A-C and A'-C', black arrows), while epiblast cells in the primitive streak were still connected to the rest of the epiblast with the onset of gastrulation (Figure 2 G-H and G'-H', white open arrowheads). These cells changed their shape from tall column to triangle, lost the epiblast cell–basement membrane interaction, and were squeezed together. During gastrulation, we found that cells ingress through the PS, break down the basement membrane, and invade into the space between the hypoblast and epiblast to form the intraembryonic mesoderm (Figure 2 E-H and E'-H', black open arrowheads). There were also cells that migrated posterolaterally beyond the embryonic disc border to form extraembryonic mesoderm (Figure 2 F-H and F'-H', white arrows). Thus, the epiblast undergoes a drastic morphological transition, engaging intra/extraembryonic mesoderm cells into a migratory behavior.

258

259 Notably, some gastrulating cells posterior to the leading edge of the mesoderm
260 wrings were found to undergo mesenchymal epithelial transition (MET), the
261 reverse mechanism of EMT, as they intercalate into the overlying hypoblast
262 (visceral endoderm) epithelium to form the gut endoderm on the surface of the
263 embryo (Figure 2 E'-G', K'-L' and Figure 3 C'-E',K'-M', black arrowheads).
264 These MET cells, with obvious mesenchymal characteristics, were larger than
265 the pre-existed hypoblast cells but were not in a dominative presence. As
266 previously reported that there were two populations of definitive endoderm cells
267 in human gastrulation embryos by single cell transcriptome analysis (Tyser et
268 al., 2020), this may suggest that the mixing of these two (embryonic and
269 extraembryonic) endodermal populations collectively comprises the definitive
270 gut endoderm, as they do in the mouse embryo (Viotti et al., 2014).

271

272 Next, to address the intricate morphogenesis of the developing primate embryo,
273 the three-dimensional (3D) anatomical atlas was performed based on serial
274 sections with the collected gastrulation embryos. In line with knowledge from
275 3D reconstruction of human specimen, we found that the epiblast of
276 Cynomolgus monkey changed from a globe-like into a disc-like shape, with the
277 primitive streak in the midline (Figure 2N-O and Figure 3K, P). Afterwards, the
278 flat disc shape was distorted as the embryonic cavity increases and perfect
279 morphology is difficult to be preserved without perfusion (Figure 3 O, P and S5).
280 At the end of gastrulation, the embryo which begins as a flat sheet of cells, folds
281 to acquire a typical cylindrical shape (Figure 4 and S6). The ectoderm
282 developed into neural ectoderm and surface ectoderm, then neural ectoderm
283 underwent bending to create the neural folds, which converge towards the
284 dorsal midline (Figure 4 A-C and E) (Nikolopoulou et al., 2017). The mesoderm
285 continually developed in the tail bud (Figure 4 D), and divided into the paraxial

286 mesoderm, intermediate mesoderm, and lateral plate mesoderm (Figure 4 C)
287 (Tani et al., 2020). The paraxial mesoderm gives rise to the somite, a notable
288 feature of early organogenesis, mainly through somitogenesis (Lawson and
289 Wilson, 2016). Besides, somite count is a convenient means to stage embryos,
290 and there were 5 or 6 somites visible at E21, corresponding to CS9 of human
291 embryo development (Figure 4 C and E). After gastrulation, the gut endoderm
292 was regionalized along the dorsal-ventral (D-V) and anterior-posterior (A-P)
293 axes into broad foregut, midgut, and hindgut domains. In the monkey embryos,
294 we observed that the foregut pocket invaginated to generate the anterior
295 intestinal portal, while the hindgut pocket at the posterior formed the caudal
296 intestinal portal, a process similar to that in the mouse embryo development
297 (Figure 4 E and S6) (Nowotschin et al., 2019). Together, we reconstructed the
298 histologic detail based on more than 100 serial high-quality sections and
299 provided a digitalized anatomy atlas for the Cynomolgus gastrulation monkeys
300 which can serve as valuable reference for primate embryogenesis.
301

302 Molecular architecture of the gastrulating monkey embryo

303 Previously, we conducted a spatiotemporal transcriptome on the mouse embryo
304 by low-input Geo-seq during gastrulation from E5.5 to E7.5 stages (Peng et al.,
305 2019). To achieve a spatial molecular profiling of primate embryos during
306 gastrulation, we applied Geo-seq to analyze the expression of genes in
307 embryonic and extraembryonic tissues at E18 and E20 (Figure 5A and S7A-C,
308 STAR Methods). Although the tissue morphology of cryo-sections was inferior
309 to paraffin embedding sections, the germ layers were discernable. We divided
310 the embryonic tissues into the upper, middle and lower layer (Em-Up, Em-Mid
311 and Em-Low) according to the dorsal-ventral axis based on the anatomical
312 structure. Furthermore, extra-embryonic mesenchyme 1 and 2 (EXMC1/

313 EXMC2) and yolk-sac parietal endoderm (YE1) and extraembryonic
314 mesemchyme lining the yolk sac (YE2) were captured from extraembryonic
315 tissues according to their locations in the amniotic cavity and secondary yolk
316 sac (Figure S7A-C). The spatial transcriptome of primate gastrulating embryos
317 provides a high- depth and quality dataset, with ~15M mapped reads, ~87%
318 mapping ratio, and 12,000 genes on average (Figure S7F). The consistency
319 between two replicates or developmental stages was more than 0.94, indicating
320 we can rely on these data to probe the molecular architecture of the primate
321 embryo (Figure S7F). We further generated a dot plot to facilitate the planar
322 (top represents dorsal and bottom represents ventral) display of the spatial
323 expression of the combined gastrulating primate embryos, which called STGE-
324 plot (Spatial Transcriptome of Gastrulating Embryos), according to the
325 geography and morphology of qualified samples (n=86) (Figure 5A).
326
327 Next, we performed principal component analysis (PCA) and uniform manifold
328 approximation and projection (UMAP) of the tissue samples with unsupervised
329 clustering, and the result showed tight clustering of samples by spatial positions
330 (Figure 5B), pointing to a location-dependent germ layer specification. To
331 characterize the functional status of gene regulatory network (GRN), we
332 performed SCENIC (single-cell regulatory network inference and clustering)
333 (Aibar et al., 2017) analysis (STAR Methods). The specifically enriched regulon
334 activity based on transcription factors and their co-expressed target genes was
335 further grouped into 11 modules that are specifically activated in seven spatial
336 cell clusters (Figure 5 C and E). In line with the unsupervised clustering of
337 transcriptome, the regulon-based dimensionality reduction showed that the
338 tissue type and spatial location were clearly delineated on the top three PC
339 axes (Figure 5C). The PC1 axis defined cell types of embryonic and extra-
340 embryonic tissues, and the PC2 and PC3 axis represented the spatial variances.

341 Therefore, the signatures of tissue types and geographical regions of
342 Cynomolgus monkey gastrulating embryos were distinguished by both gene
343 expression and regulatory activity.
344
345 To investigate the lineage identities of spatial samples, we incorporated key
346 marker genes, regulon activities, geographical anatomy and cell-type
347 deconvolution to infer spatial molecular organization of primate gastrulation.
348 For cell-type deconvolution in spatial transcriptome, SPOTlight that based on a
349 non-negative matrix factorization (NMF) regression algorithm was used to infer
350 the location of cell types (Elosua-Bayes et al., 2021). We integrated both in vivo
351 single cells (Nakamura et al., 2016) and our spatial transcriptomics data of
352 monkey gastrulating embryo, and demonstrated that gastrulating cells (Gast1,
353 2a and 2b) were mainly located in middle and lower layer of embryonic disk
354 whereas the post-implantation late epiblast cell (PostL.EPI) account for the
355 largest proportion in the upper layer of embryo (Figure S7D). In line with cell-
356 type deconvolution analysis, the correlation coefficiency of gene expression
357 showed that the upper layer of embryonic tissues was more similar to the
358 epiblast cells, whereas there was a discrete regional property of embryonic and
359 extra-embryonic cell types (Figure S7E). In addition, the spatially captured
360 tissue from gastrulating monkey embryos were consistent with cells of human
361 CS7 gastrula (Figure 5D). Human epiblast like cells mainly located in Em-Up,
362 primitive streak cells were including in Em-Mid, while extra-embryonic
363 endoderm cells were separated into Em-Low, YE1 and YE2.
364
365 We identified marker genes and regulatory networks that are critical for the
366 molecular annotation of the spatial samples and found there is a considerable
367 conservation between species. For example, the *POU5F1*, *HESX1*, *SOX2* and
368 *NANOG* pluripotency regulatory network were highly activated in embryonic

369 tissues, particularly in the upper layer which are epiblast and its derivatives
370 (Figure 5E), corroborating previous findings (Boroviak et al., 2018) (Nakamura
371 et al., 2016; Niu et al., 2019; Xiang et al., 2019) (Figure S7J and K). Notably, in
372 contrast to that in the rodent model, *NANOG* and *PRDM14* were still highly
373 expressed in the embryonic tissues until the middle and late stages of
374 gastrulation in primate, suggesting a distinct spectrum of pluripotency during
375 gastrulation.
376
377 We found that the PS-related genes *TBXT*, *MIXL1* and *FOXA2* showed high
378 expression in the Em-Mid and Em-Low of the epiblast, but was low in the yolk
379 sac endoderm and extra-embryonic mesenchyme (Figure S7J). Similarly, the
380 G4 regulon, consisting of MIXL1, EOMES, FOXA2 and SOX17, were
381 specifically activated in the Em-Low and Em-Mid regions and were enriched
382 with terms such as “Endodermal cell differentiation” and “Regionalization”
383 (Figure 5E). In line with the anatomical annotation, spatial territory of epithelial
384 to mesenchymal transition (EMT) genes demonstrated that epiblast cells at this
385 region undergo an EMT during gastrulation (Figure S7K). Furthermore, the
386 activating activity of the WNT and NODAL signaling pathways were
387 predominantly enriched (Figure 5F and S7K). Em-Low and Em-Mid were
388 distinguished by their relative expression of G1 regulon which were enriched in
389 chromatin remodeling, such as SP1 and KDM4B, suggesting that epigenetics
390 has a pivotal role in lineage commitment (Nicetto et al., 2019; Wang et al., 2018).
391 Therefore, we classified the middle and lower layer of embryo into PS1 and
392 PS2, which may denote gastrulating cells of slightly different status.
393
394 Interestingly, the yolk-sac tissues (YE1 and YE2) showed the least similarity to
395 the other dissected regions, as revealed both by UMAP and hierarchical
396 clustering (Figure 5B and S7H). α-fetoprotein (*AFP*), transthyretin (*TTR*) and

397 albumin (*ALB*) were highly expressed in YE1 and YE2, and they also formed
398 co-expression module (Figure S7I and J). The expression of *AFP*, *TTR* and
399 *ALB* was usually regarded as the earliest marker of hepatoblasts (Gualdi et al.,
400 1996; Sheaffer and Kaestner, 2012), while the yolk sac may serves as a pivotal
401 organ for diverse functions of intestine, liver, bone marrow and thyroid even
402 before the matured organs have not been generated at the early embryo
403 development stages (Ross and Boroviak, 2020; Wong and Uni, 2021).
404 Additionally, the apolipoprotein gene family members were also specifically
405 expressed in yolk-sac endoderm, such as *APOA1* (Figure S7J), *APOA2/4* and
406 *APOC2/3* (from DEGs, data not show), which is consistent with the function of
407 the yolk sac as the primary site of apolipoprotein synthesis during early primate
408 and mouse development (Baardman et al., 2013; Cindrova-Davies et al., 2017).
409 Furthermore, as previously reported that primate yolk sac delivers nutrients and
410 oxygen to the embryo early in development (Cindrova-Davies et al., 2017; Dong
411 and Yang, 2018; Exalto, 1995), pathway activity analysis and weighted gene
412 co-expression network analysis (WGCNA) showed that reactome of oxygen
413 release and AMI pathway involving collagen (*COL4A1/2/3/4/5/6*), fibrinogen
414 (*FGA, FGB* and *FGG*) and serpin members (*SERPINC1*) were enriched
415 exclusively in the yolk sac tissues (Figure S7I and K). Notably, we identified
416 FOXA1, FOXA3 and NR1H4 as the key transcript factors in maintaining the
417 identities of yolk sac endoderm (Figure 5E and H) and have the most
418 connections within the regulon group and the node-regulons. Previously,
419 FOXA1 was defined as the visceral/yolk-sac endoderm (VE/YE) marker
420 (Nakamura et al., 2016), hence our analysis further indicated that FOXA1 and
421 FOXA3 correlate with yolk sac endoderm fate specification, whereas FOXA2
422 were functionally critical for mesoderm and definitive endoderm development
423 (Figure 5E and H).
424

425 Cellular fate specification depends on temporally and spatially precise cell
426 communication, so we performed intercellular communication analysis based
427 on ligands, receptors and their cofactors by CellChat (Jin et al., 2021). Although
428 not at single-cell resolution, the cell-cell communication network identified PS1
429 cells as the dominant communication “hub” (Figure 5G). PS1 cells were mainly
430 enriched with WNT and NOTCH signaling pathway in a paracrine and autocrine
431 manner (PS1 and PS2), which is consistent with their known roles (Figure 5G)
432 in gastrulation (Nakamura et al., 2016; Souilhol et al., 2015). In agreement with
433 previously work in mouse (Ciruna and Rossant, 2001; Sun et al., 1999), we
434 identified that PS1 was the primary FGF source in primate, signaling both in
435 autocrine and paracrine manner with FGF15 − FGFR1, FGF17 − FGFR3 and
436 FGF17 − FGFR1 ligand-receptor pairs to drive the migration of delaminated
437 cells and the differentiation of the mesendoderm.
438
439 To uncovered the key sequential signaling events along the process of primate
440 gastrulation, we combined the communication pattern analysis with the
441 previously studied cell events in mouse and human cell models. It’s known that
442 the BMP signaling in the extraembryonic ectoderm in mouse was the source of
443 signaling molecules that transduce the fate of proximal epiblast cells, which
444 formed the primitive streak subsequently (Ben-Haim et al., 2006; Brennan et al.,
445 2001; Chhabra et al., 2019; Rivera-Perez and Hadjantonakis, 2015; Rivera-
446 Perez and Magnuson, 2005). In contrast to mouse, primate embryos form the
447 extraembryonic mesoderm prior to gastrulation, and the BMP signaling was
448 highly enriched in the extraembryonic mesoderm (Figure S7K), suggesting that
449 the extraembryonic mesoderm may serve as a source of signaling molecules
450 in initiation of primate gastrulation. Notably, Hippo-Yap signaling was highly
451 activated in the extraembryonic mesoderm (Figure 5F). Previous work has
452 highlighted the Hippo signaling in regulating early endoderm development

453 during mouse gastrulation (Peng et al., 2019) and the crosstalk between TAZ
454 and SMAD (Varelas et al., 2008), therefore the co-localization of BMP and
455 Hippo/Yap signaling in the extraembryonic mesoderm may hint that Hippo-Yap
456 interacts with BMP signaling to initiate gastrulation of primate. Remarkably,
457 insulin-like growth factor (IGF) signaling was prominently secreted from EXMC2
458 cells to PS1 cells, and autocrine and paracrine loops of prokineticins (PROK)
459 were established between PS1 and PS2 in monkey gastrulating embryo (Figure
460 5G and S7L). IGF signaling pathway has been highly conserved and plays an
461 important role in early mesoderm formation of zebrafish and rabbits, which
462 influences the expression of *Otx2*, *FGF8*, *BMP2b*, *Wnt3a* and *Brachyury* (Eivers
463 et al., 2004; Thieme et al., 2012). In addition, IGF1 induced EMT process
464 through the activation of NFκB by the PI3K pathway, then induce SNAIL1
465 stabilization (Lamouille et al., 2014; Singh et al., 2018). Together, we predicted
466 that BMP, Hippo-Yap and IGF signaling pathway would be imperative to initiate
467 gastrulation in primate, and the communication pattern of CXCL, BTLA, LIGHT
468 and APJ is also from the EXMC to the PS1 specifically (Figure 5G).
469

470 Cellular and molecular dynamic of macaque gastrulation

471 To further confirm the observed characteristics of germ layer differentiation, the
472 expression of germ layer-specific molecular markers at RNA and protein levels
473 were investigated (Figure 6A and B). Consistent with previous reports, OCT4
474 (*POU5F1*) was exclusively expressed in the pluripotent cells, especially in the
475 epiblast and ectoderm of early or late gastrulation. GATA6 was specifically
476 detected in the hypoblast by immunohistochemical staining. Notably, we found
477 that the EMT cells were weakly positive for OCT4 and strongly express T, a
478 marker for primitive streak or nascent mesoderm. Interestingly, some
479 mesenchymal cells with the weak expression of T intercalated in the hypoblast

480 (Figure 6 B, white arrowheads), as shown in the histological images analyzed
481 previously (Figure 2 and 3), suggesting a prerequisite for downregulation of the
482 primitive streak genes in forming the definitive endoderm. Furthermore, spatial
483 gene expression showed that *NANOG* still marks pluripotent cells in the epiblast
484 (Figure 6 A and S7J). Taken together our three-dimensional gastrulating model
485 (Figure 6C) provides new insights for the molecular architecture of primate
486 gastrulation.
487

488 Cross-species spatiotemporal transcriptome analysis of 489 mammalian gastrulation development

490 Gastrulation is a fundamental morphogenetic process in development, and the
491 key signaling pathways that regulated the establishment of germ layers were
492 evolutionarily conserved, such as the role of WNT, NODAL and BMP signaling
493 pathways in non-human primate and rodent mammalians. However, there are
494 significant difference between primates and mice in both morphology and
495 development rate of gastrulation. To systematically reveal the molecular
496 signatures associated with different mammalian species, we performed cross-
497 species comparative analysis on the spatiotemporal transcriptome in mouse,
498 Cynomolgus monkeys and human gastruloid (STAR Methods). We showed that
499 the states of Cynomolgus monkey at E18 and E20 were resembling to the
500 middle-late stage of mouse gastrulation (Figure 7A and S8A). We aligned the
501 regulons along the developmental time and obtained 5 clusters that correspond
502 to the dynamic patterns of cell fate commitment and regionalization (Figure
503 S8B). All these dynamic regulons (n=451) across gastrulation were subjected
504 to dimensionality reduction analysis. The PCA plot showed that the cell types
505 between monkey and mouse were clustered together, suggesting a germ lay
506 consistency (Figure 7B). The PS1 and PS2 in macaque gastrulating embryos

507 were close to the mouse mesoderm and endoderm, respectively. To explore the
508 species-specific molecular mechanism underlying the germ layer segregation,
509 we defined a species/spatial domain-specificity score (SSS) based on Jensen-
510 Shannon divergence (STAR Methods). The activities of most regulons (more
511 than 50%) were similar during germ layer formation in mice and monkeys,
512 suggesting that the major gastrulation events are conserved and common
513 molecular regulatory mechanisms are shared between species (Figure 7C-E,
514 S8C-E, Table S3). Next, we looked into the species difference in germ layers
515 and whole embryonic tissues (Figure 7C-F). For quantitative visualization of
516 species specificity, relative SSS of regulons were plotted in ternary plot (Figure
517 7F). The activity of KLF7 were preferred in mouse, especially in the ectoderm
518 and the endoderm differentiation (Figure 7C, E and F), whereas the ELF3 were
519 enriched in the ectoderm of macaque (Figure 7C and F). Given that *Klf7* had
520 inhibitory activity on mesoderm (Gao et al., 2015) and *Elf3* was a negative
521 regulator of epithelial-mesenchymal transition in gastrulation and tumor
522 metastasis (Scheibner et al., 2021; Yeung et al., 2017), this might imply that
523 mice and non-human primates use functionally similar but different regulatory
524 factors in the maintenance of the ectoderm epithelium.
525
526 Interestingly, we found that Forkhead box transcription factor of subclass O
527 (FOXO) family showed species-dependent activity. Specifically, we showed that
528 FOXO1 was exclusively activated in macaque gastrulating embryos and mouse
529 embryos exhibited the highest levels of FOXO4 regulons, while FOXO3 activity
530 was substantially elevated in human (Figure 7G-H). In line with that FOXO1
531 regulates core pluripotency factors in human and mouse embryonic stem cells
532 by promoting the expression of *OCT4* and *SOX2* (Zhang et al., 2011), we found
533 that FOXO1 have a strong positive correlation with stem cell pluripotency genes
534 *SOX2* and *ZSCAN10*, which enriched in negative regulation of cell

differentiation and transcriptional regulation of pluripotent stem cells (Figure S8F). Furthermore, we identified the targets of FOXO1/3/4 and their top related genes. They also showed species differences with FOXOs expression, including *TERT* (telomerase reverse transcriptase), *BCL6* and *TEF* (thyrotroph embryonic factor) in mouse, macaque and human embryos respectively (Figure S8H-J) (Chakravarti et al., 2021; Tang et al., 2002; Yamashita et al., 2014; Yang et al., 2019). Together, our data indicate that FOXOs may play a vital role in interspecies differences during gastrulation. Considering the prominent role of FOXO family in metabolic homeostasis and organismal longevity, the species-specific mechanisms may imply profound effect of FOXO in even beyond embryo gastrulation.

Discussion

In this study, we have provided an anatomical atlas and molecular database spanning the entire gastrulation to the early organogenesis period of Cynomolgus monkey development. This analysis was a critical step in understanding of human embryology within similar time-window, which remain largely unknown due to technical difficulties and ethical issues. First, we have captured a series of high-resolution tissue anatomical sections from early gastrulation (E17) to early organogenesis (E21), revealed the dynamic changes of cell histomorphology and cell proliferation kinetics, and discovered the critical role of cell migration and EMT/MET transformation in the process of germ layers formation. Secondly, the three-dimensional model of primate embryos was reconstructed to analyze the dynamics of gastrulation from a holistic perspective. Furthermore, the spatial transcriptome of macaque gastrula has been performed. We identified the key regulons and their interaction networks

561 in different cell types in the process of germ layer segregation. Finally, we have
562 explored cross-species differences in mouse, Cynomolgus monkeys and
563 human by comparatively analyzed the spatiotemporal transcriptomes.
564
565 Gastrulation is a period of rapid growth, proliferation and differentiation. Several
566 morphological and genetic reports in mouse have shown that the cell cycle
567 progression is coordinated with transcription, cell migration, and cell
568 differentiation (Abe et al., 2013; Mitiku and Baker, 2007; Snow, 1977; Tam and
569 Behringer, 1997), while little is known about this in primate gastrulation. We
570 have applied detailed histological analyses to assess the growth rate by
571 determining the cell number increase, and highlighted the cell proliferation
572 kinetics in primate gastrulation. However, the tissue- and embryo-wide division
573 patterns in primate gastrulating embryos needs further to be studied through
574 genetic markers labeling and spatial omics, because the rate of proliferation
575 differs significantly across the different regions of the epiblast in mouse at
576 gastrulation stages (McDole et al., 2018; Snow, 1977).
577
578 Although the morphology of primate embryonic development has been studied
579 for at least a century (de Bakker et al., 2016; Grobstein, 1985; Hendrickx, 1972;
580 Luckett, 1978), detailed anatomical imaging with high temporal resolution in
581 primate gastrulating embryos are lacking. We provided an atlas with sequential
582 stages and serial sections of gastrulating embryos in 2D and 3D, which was
583 fundamental to reveal cellular morphological changes during ectoderm,
584 mesoderm and endoderm formation. The results of this study showed that
585 mesenchymal like cells were found intercalated in hypoblast individually, not as
586 a coordinated sheet to displace the original hypoblast (Figure 2 and 3). And
587 immunohistochemical staining indicated that embedded mesenchymal cells
588 weakly expressed the primitive streak marker T (Figure 6B), implying that the

589 original hypoblastic cells could become integrated into the newly formed
590 embryonic endodermal layer and EMT/MET play important roles in the
591 embryogenesis of primate endoderm.
592
593 Remarkably, from the spatial transcriptome of monkey gastrulating embryos,
594 FOXA subfamily was found to have important biological functions in embryonic
595 and extraembryonic endoderm specification (Figure 5E and H). From the
596 evolution and phylogeny view, FOXA genes have a conserved role in the
597 development of the derivatives of the primitive gut (Hannenhalli and Kaestner,
598 2009; Lai et al., 1991), whereas the functional diversity among FOXA proteins
599 with the spatio-temporal expression patterns were not clear. In mouse, neither
600 *Foxa1* nor *Foxa3* inactivated mutants exhibit any early phenotype (Grapin-
601 Botton and Constam, 2007; Kaestner et al., 1998), whereas they can
602 compensate for the loss of *Foxa2* in the null mutants, which allows hindgut, but
603 not foregut and midgut formation (Dufort et al., 1998; Monaghan et al., 1993;
604 Sasaki and Hogan, 1993). In detail, the *FOXA1* was not just as the yolk-sac
605 endoderm marker (Nakamura et al., 2016), but also regulate yolk sac endoderm
606 fate specification with *FOXA3*. On the other hand, *FOXA2* had a pivotal role in
607 cell fate commitment of embryonic endoderm, which was consistent with the
608 finding in single cell transcriptome of human (Tyser et al., 2020). Indeed, the
609 molecular map of cell populations at defined positions varies. Our Geo-seq
610 approach may not be able to separate the mesoderm and endoderm cells at
611 single-cell resolution, therefore results in a relatively similarity at transcription
612 level to be defined as PS1 and PS2, respectively (Figure 5E). Further research
613 should be undertaken to explore the spatiotemporal molecular architecture at
614 single cell resolution and to investigate the mechanism of gut endoderm
615 formation in nonhuman primates.
616

With the spatial transcriptome data of Cynomolgus embryos, we can now glean the primate-specific molecular program by cross-species comparative analysis. We defined species-specific regulons. As expected, most regulons were shared in mice and monkey embryos during germ layer formation, suggesting that the gastrulation event were evolutionally conserved. Interestingly, we found FOXO family showed species-specific usage during gastrulation. FOXO1, FOXO3 and FOXO4 were enriched in macaque, human and mouse respectively (Figure 7G-H), demonstrating that FOXOs may have crucial functions in interspecies evolution. As a key transcription factor to integrate different signals from the insulin/ insulin-like growth factor 1 (IGF-1) signaling pathway, target of rapamycin (TOR) signaling, AMP-activated protein kinase (AMPK) pathway and Jun N-terminal kinase (JNK) pathway (Fontana et al., 2010; Lin et al., 1997; Ma and Gladyshev, 2017; Sun et al., 2017; Tian et al., 2017) to participate in a wide range of important cellular processes such as cell cycle arrest, apoptosis, and metabolism besides its function in stress resistance and longevity (Calissi et al., 2021; Eijkelenboom and Burgering, 2013; Golson and Kaestner, 2016). The preferred cellular mechanisms of FOXO family during early embryo development and beyond is awaiting further investigation.

In summary, our study provides a morphological and molecular atlas for illustrating the dynamics of key processes and regulatory mechanisms during three germ layers formation in primate embryos. Knowledge gained from this work should be valuable for evaluating the interspecies difference and setting a reference for in vitro mimic of monkey embryogenesis. Our work also provide a reasonable working model for human gastrulation. To fully dissect the primate gastrulation, additional studies will be needed to build the single-cell spatiotemporal molecular maps with implementing genetic manipulation and lineage tracing on monkey models.

Figure

Figure 1

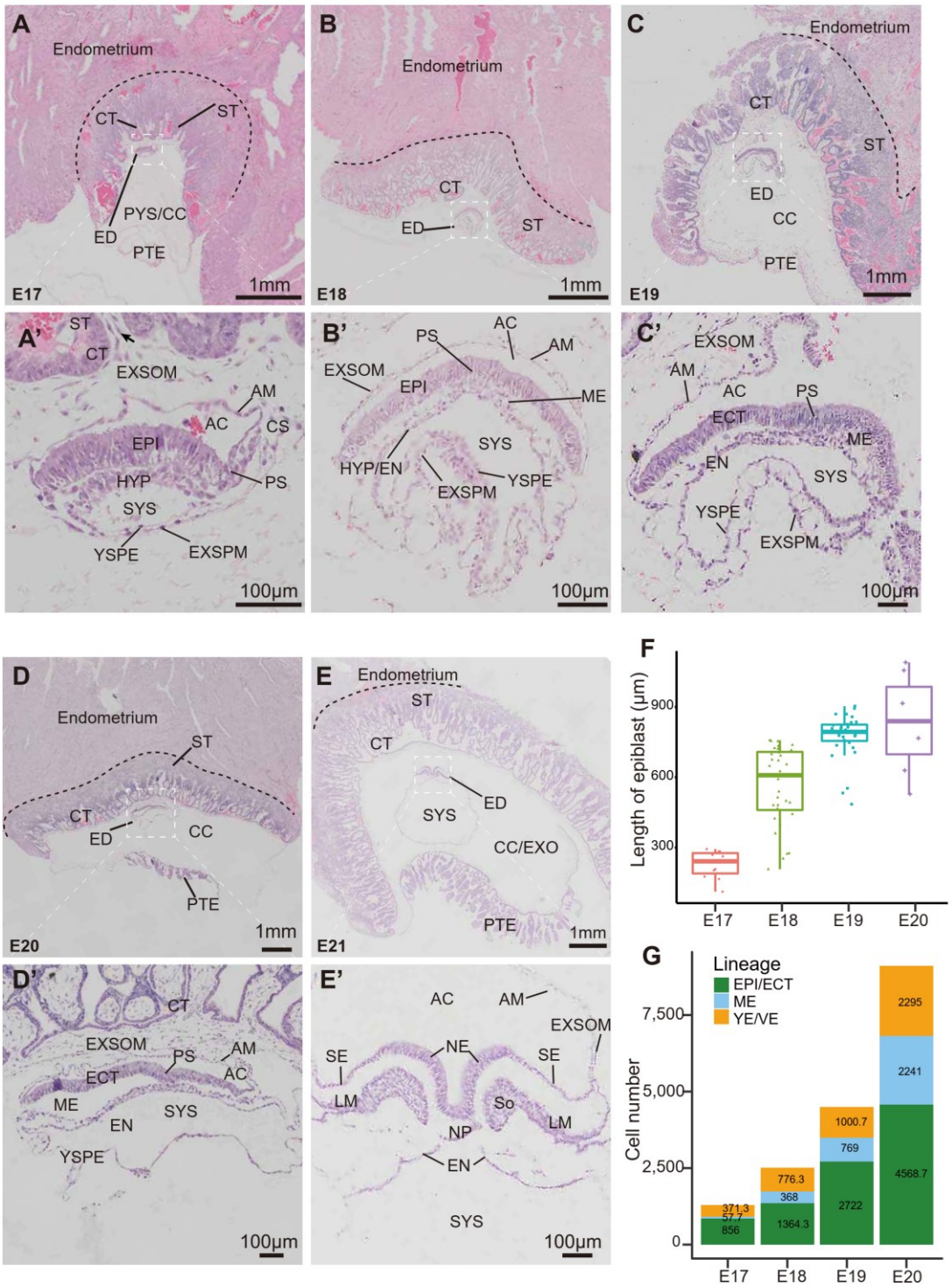

648 **Figure 1 Overview of monkey gastrulation development.**

649 A-E, Haematoxylin and eosin staining of the sections of macaque gastrulating
650 embryos at E17 (A and A'), E18 (B and B'), E19 (C and C'), E20 (D and D') and
651 E21 (E and E'). The image at bottom is a higher magnification of the area boxed
652 on the top. Black arrow points to the extraembryonic mesenchyme has invaded
653 to form the secondary villi. ST, syncytiotrophoblast; CT, cytotrophoblast; PYS,
654 primary yolk sac; CC, chorionic cavity; EXO, exocelom; PTE, parietal
655 trophectoderm; ED, Embryonic disc; EXMC, extra-embryonic mesenchyme cell;
656 AC, amniotic cavity; AM, Amnion; CS, connecting stalk; EPI, epiblast; ECT,
657 ectoderm; PS, primitive streak; ME, mesoderm; HYP, hypoblast; EN, endoderm;
658 YSPE, yolk-sac parietal endoderm; EXSPM, extraembryonic splanchnic
659 mesoderm; EXSOM, extraembryonic somatic mesoderm; SYS, secondary yolk
660 sac.
661 F, The embryo sizes were assessed by the length of sectioned epiblast.
662 G, Bar plot showing total cell numbers in the embryonic germ layers during
663 gastrulation stages. Color represents the germ layer.
664

665 Figure 2

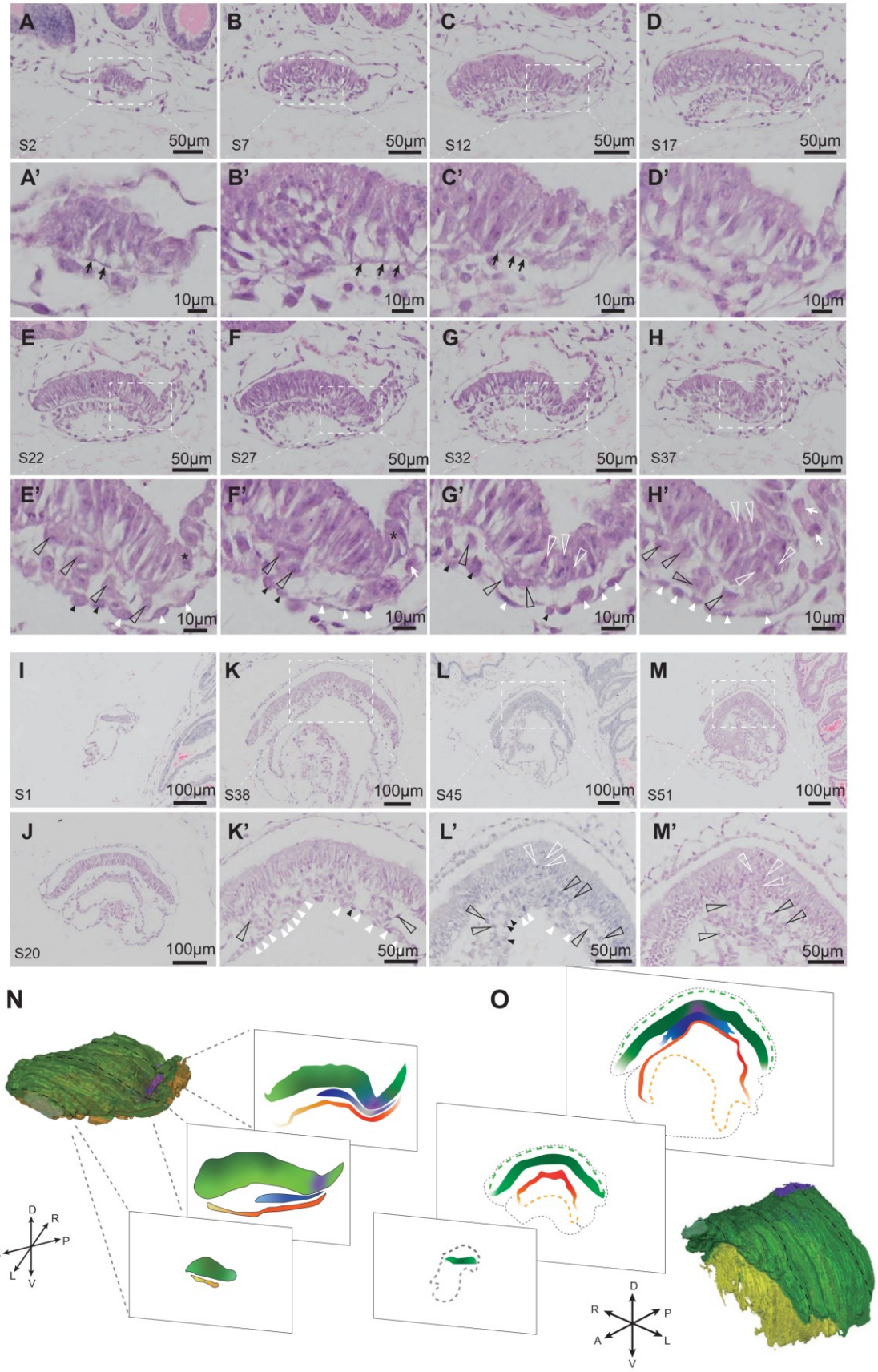

666

667 **Figure 2 Geography of early gastrulation stages in monkey embryos**

668 A-M, Haematoxylin and eosin staining of the sections of macaque gastrulating
669 embryos at E17 (A-H and A'-H') and E18 (I-M and K'-M'). The number of the
670 section is shown in the lower left. High-magnification images are from the boxed
671 region. Black arrows point to basement membrane underlying the epiblast, and
672 white arrows point to extraembryonic mesoderm cells. White open arrowheads
673 indicate gastrulating cells in primitive steak, with black open arrowheads
674 indicating mesoderm cells. White closed arrowheads indicate hypoblast cells,
675 with black closed arrowheads indicating definitive endoderm cells that
676 intercalate in the overlying visceral endoderm epithelium. Asterisks mark
677 embryonic/extraembryonic borders. Scale bar as indicated. A, anterior; P,
678 posterior; L, left; R, right; D, dorsal; V, ventral.
679 N-O, Three-dimensional view of the reconstructed embryo highlighting the
680 primitive streak and germ layers with different colors at E17 (N) and E18 (O).
681 The black dash lines indicate the level of the transversal sections.
682

683 Figure 3

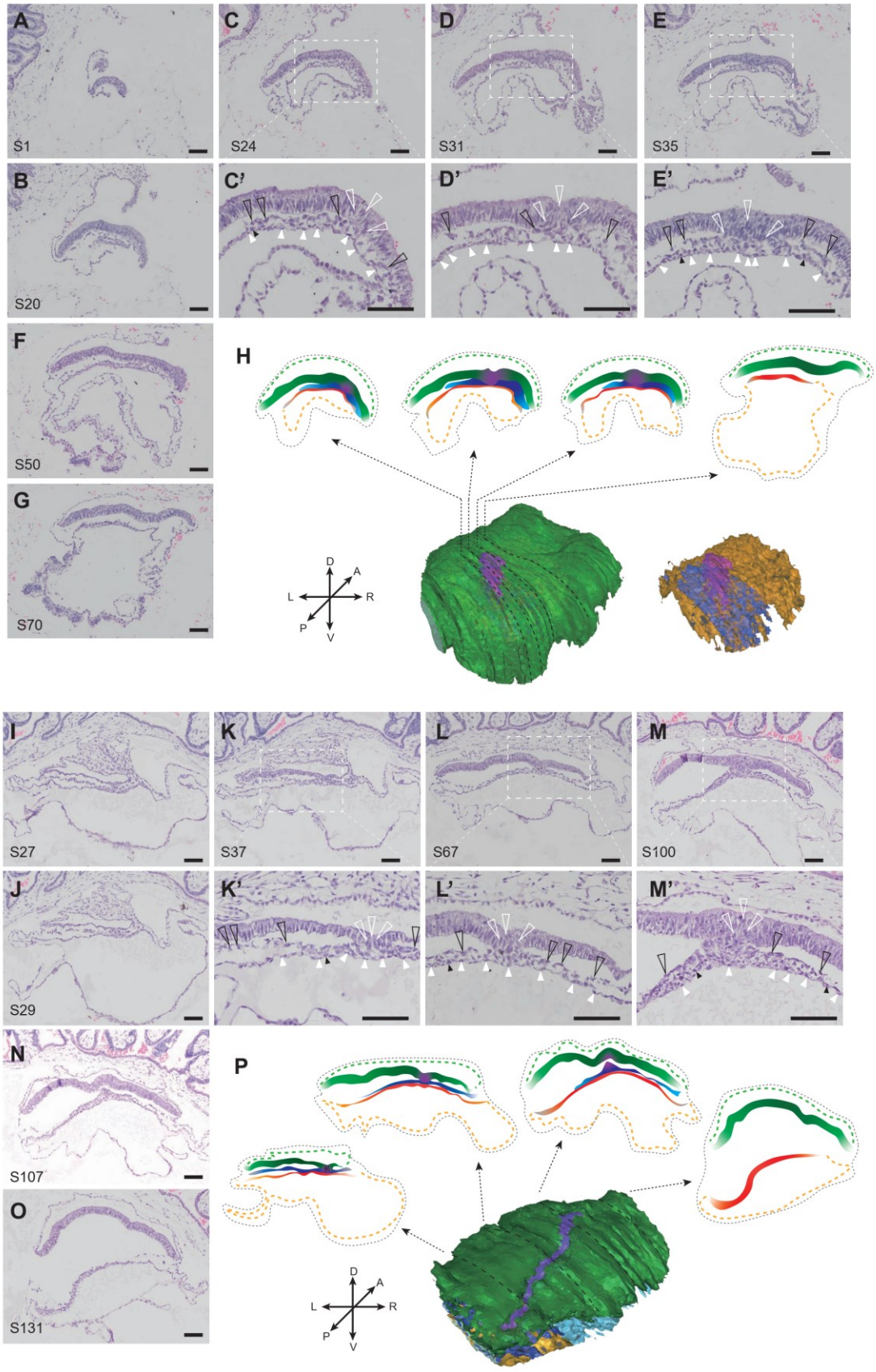

684

685 **Figure 3 Geography of late gastrulation stages in monkey embryos**

686 A-G, Haematoxylin and eosin staining of the sections of macaque gastrulating
687 embryos at E19. The number of the section is shown in the lower left. High-
688 magnification images are indicative of the boxed region. White open
689 arrowheads indicate gastrulating cells in primitive steak, with black open
690 arrowheads indicating mesoderm cells. White closed arrowheads indicate
691 hypoblast cells, with black closed arrowheads indicating definitive endoderm
692 cells that intercalate in the overlying visceral endoderm epithelium. Scale bar,
693 100μm.
694 H, Three-dimensional view of the reconstructed embryo highlighting the
695 primitive streak and germ layers with different colors at E19. The black dash
696 lines indicate the level of the transversal sections.
697 I-O, Haematoxylin and eosin staining of the sections of macaque gastrulating
698 embryos at E20.
699 P, Three-dimensional view of the reconstructed embryo at E20. The black dash
700 lines indicate the level of the transversal sections.
701

Figure 4

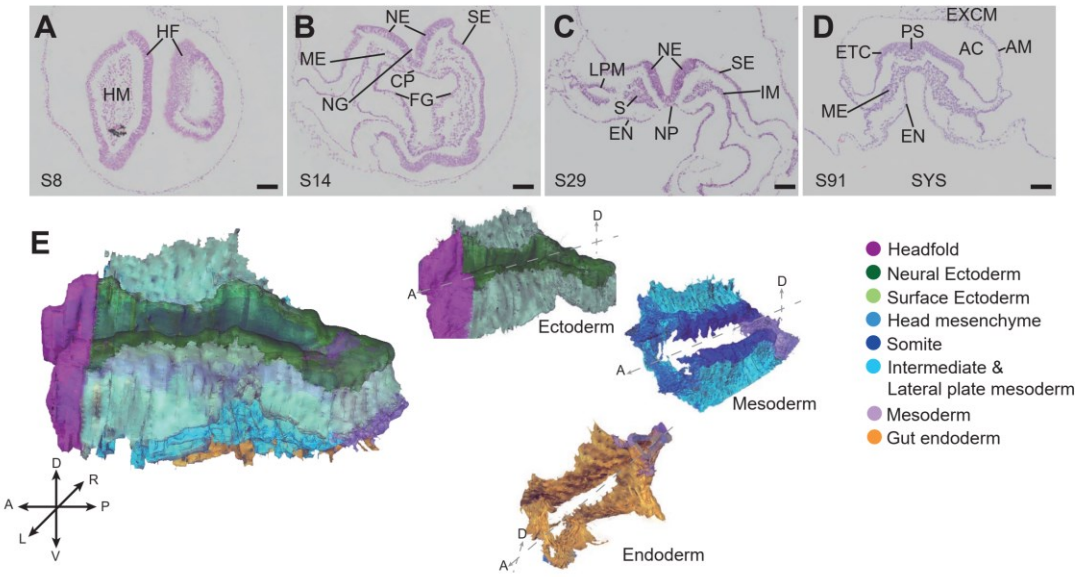

Figure 4 Morphology of primate early organogenesis

A-D, Haematoxylin and eosin staining of the sections of macaque organogenesis embryos at E21. The number of the section is signed in the lower left. HF, headfold; HM, head mesenchyme; FG, foregut; NG, neural groove; SE, surface ectoderm; NE, neural ectoderm; CP, chordal plate; ME, mesoderm; S, somite; NP, notochordal plate; IM, intermediate mesoderm; LPM, lateral plate mesoderm; EN, endoderm; PS, primitive streak; ECT, ectoderm; EXMC, extra-embryonic mesenchyme cell; AC, amniotic cavity; AM, Amnion; SYS, secondary yolk sac. Scale bar, 100μm.

E, Three-dimensional view of the reconstructed embryo at early organogenesis stage (E21). A, anterior; P, posterior; L, left; R, right; D, dorsal; V, ventral.

716 Figure 5

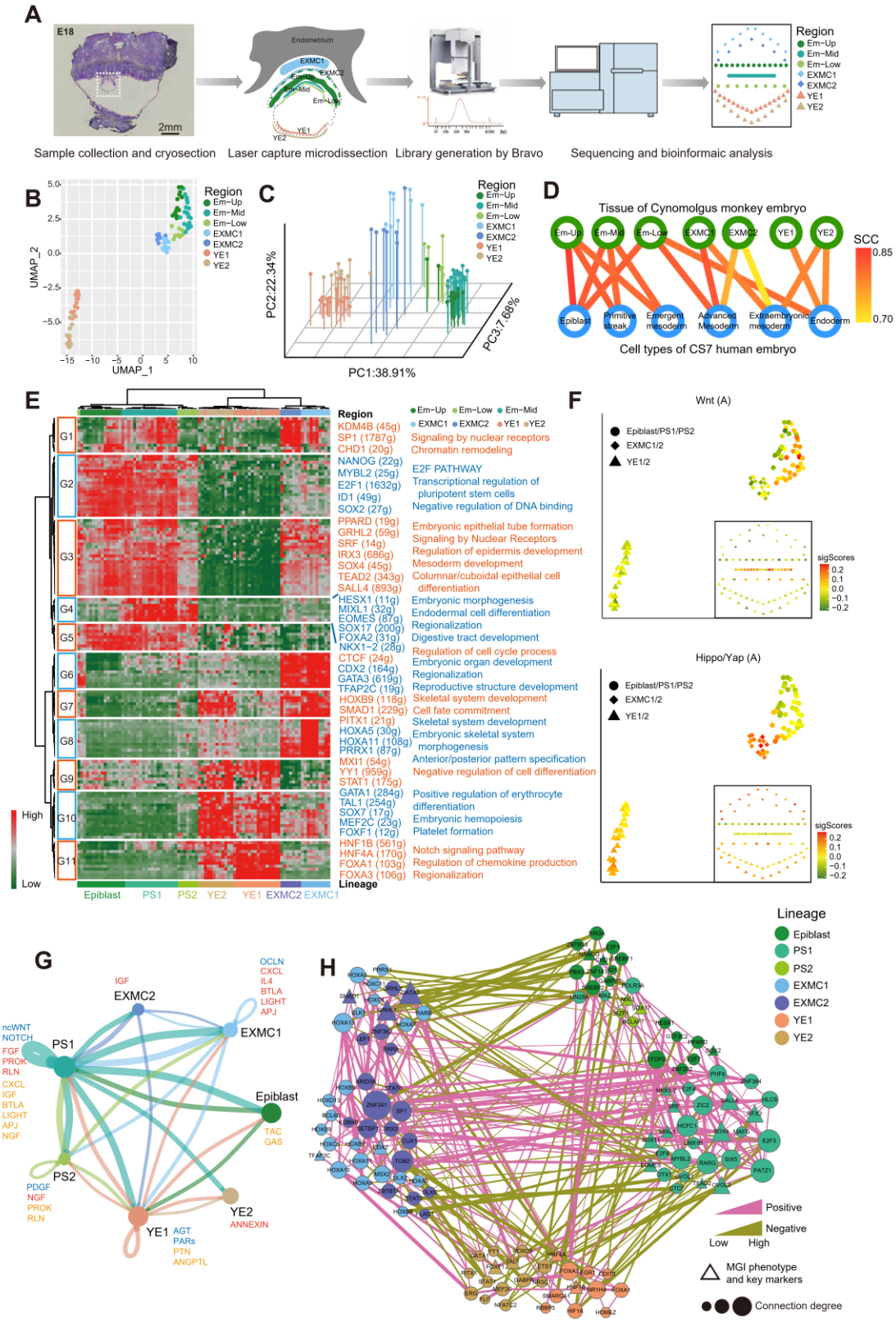

717

718 **Figure 5 Embryonic and extraembryonic spatial molecular dynamic of**
719 **gastrulating monkey embryos**

720 A, Schematic overview of spatial transcriptome of monkey embryo by Geo-seq.
721 The top to bottom of the STGE-plot represents the dorsal-ventral axis of the
722 embryo, which are extra-embryonic mesenchyme tissues (EXMC1/2),
723 embryonic disk (Em-Up, Em-Mid and Em-Low) and yolk-sac endoderm (YE1/2),
724 while left-right does not represent craniocaudal axis of embryo.
725 B, Uniform manifold approximation and projection (UMAP) embedding of
726 monkey samples based on high variable genes (n=5,000) colored by spatial
727 location (n=86).
728 C, 3D-PCA plot based on the regulon activity scores of embryonic and
729 extraembryonic samples showing separate spatial domains.
730 D, The Spearman correlation coefficient of cell population between
731 Cynomolgus monkey spatial (red module) and human single cell annotated cell
732 types (blue module) showing the location of specific cell. The color coding is
733 spearman correlation coefficient (SCC).
734 E, The heatmap of specific regulons (n=192) showing 11 regulon groups in
735 tissue samples of gastrulating monkey embryos with listing of examples of
736 regulon transcription factors (numbers of predicted target genes by SCENIC in
737 the brackets) and the enriched Gene Ontology (GO) terms for each regulon
738 group.
739 F, UMAP and STGE-plot showing the activities of the target genes related to
740 the activated states of the Wnt and Hippo–Yap signalling pathway in primate
741 gastrulation.
742 G, The weighted interaction strength between different tissue types by Cellchat.
743 The autocrine and paracrine (outgoing and incoming) signaling pathways were
744 colored by blue, red and orange respectively. Edge width represents the

745 communication probability.

746 H, The co-activation network of tissue specifical regulons based on spearman
747 correlation coefficient (SCC >0.9). The node with different colors represents the
748 highest activity tissue and the edges are the SCC value of two nodes. Violet
749 lines indicate the positive correlation and green lines indicate negative
750 correlation. A wider edge signifies higher correlation. Triangle nodes denote
751 transcription factors with mouse knockout gastrulation phenotype in MGI
752 database. The larger the node, the more connections to other regulons.

753 Figure 6

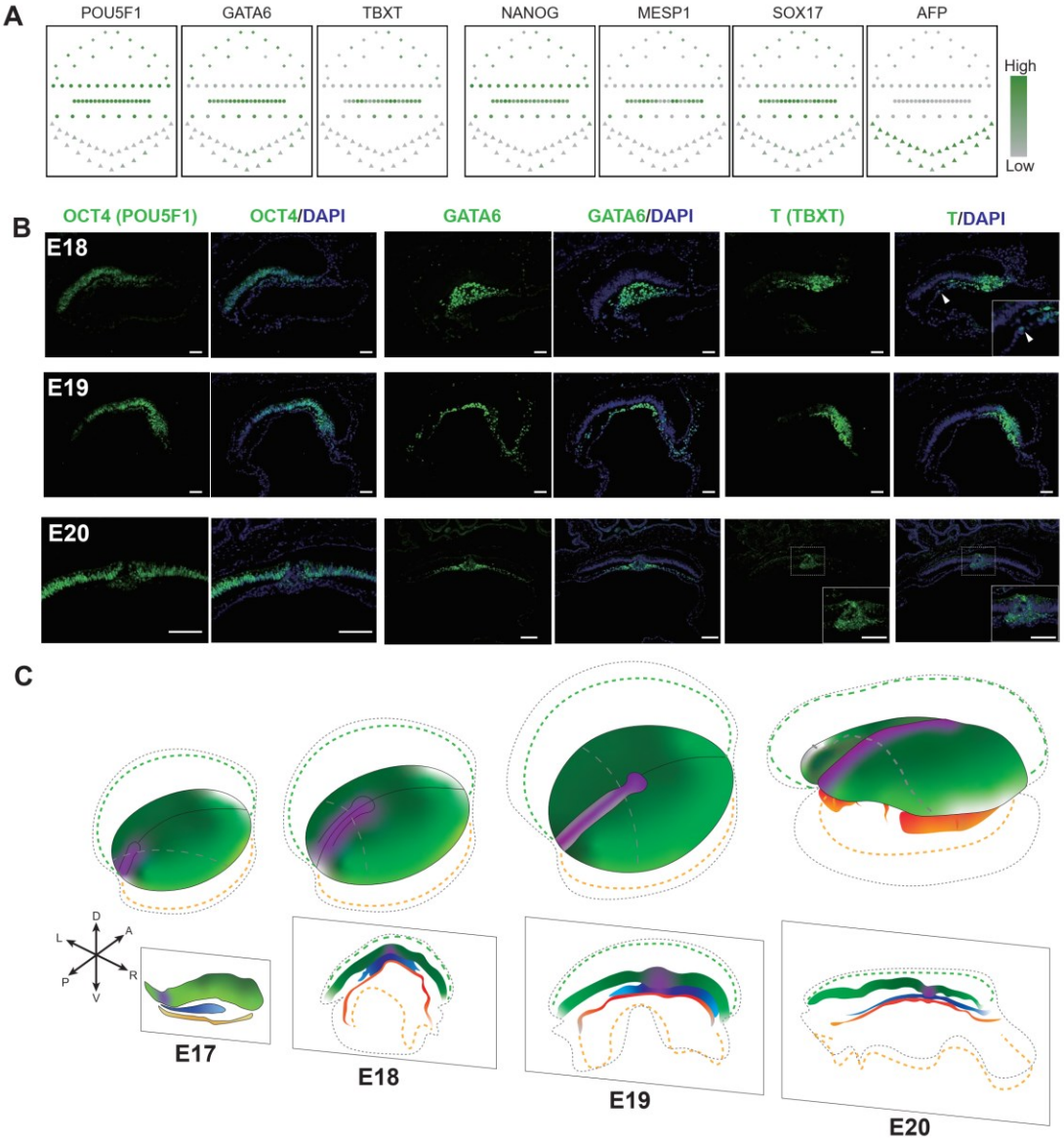

754

755

Figure 6 Spatiotemproal cellular and molecular characteristics

A, STGE-plot showing the relative expression of marker genes related to the germ layers and primitive streak in primate gastrulation. Color code represents the relative expressed levels.

B, Representative immunofluorescent images of embryos at E18, E19 and E20 for OCT4 (green), GATA6 (green), TBXT (green) and DAPI (blue). White closed arrowheads indicate gastrulating cells that intercalate in the hypoblast. High-magnification images are indicative of the boxed region. Scale bar, 100μm.

C, Scheme of monkey gastrulation development. A, anterior; P, posterior; L, left; R, right; D, dorsal; V, ventral. The grey dash lines on epiblast indicate the level of the transversal sections.

767 Figure 7

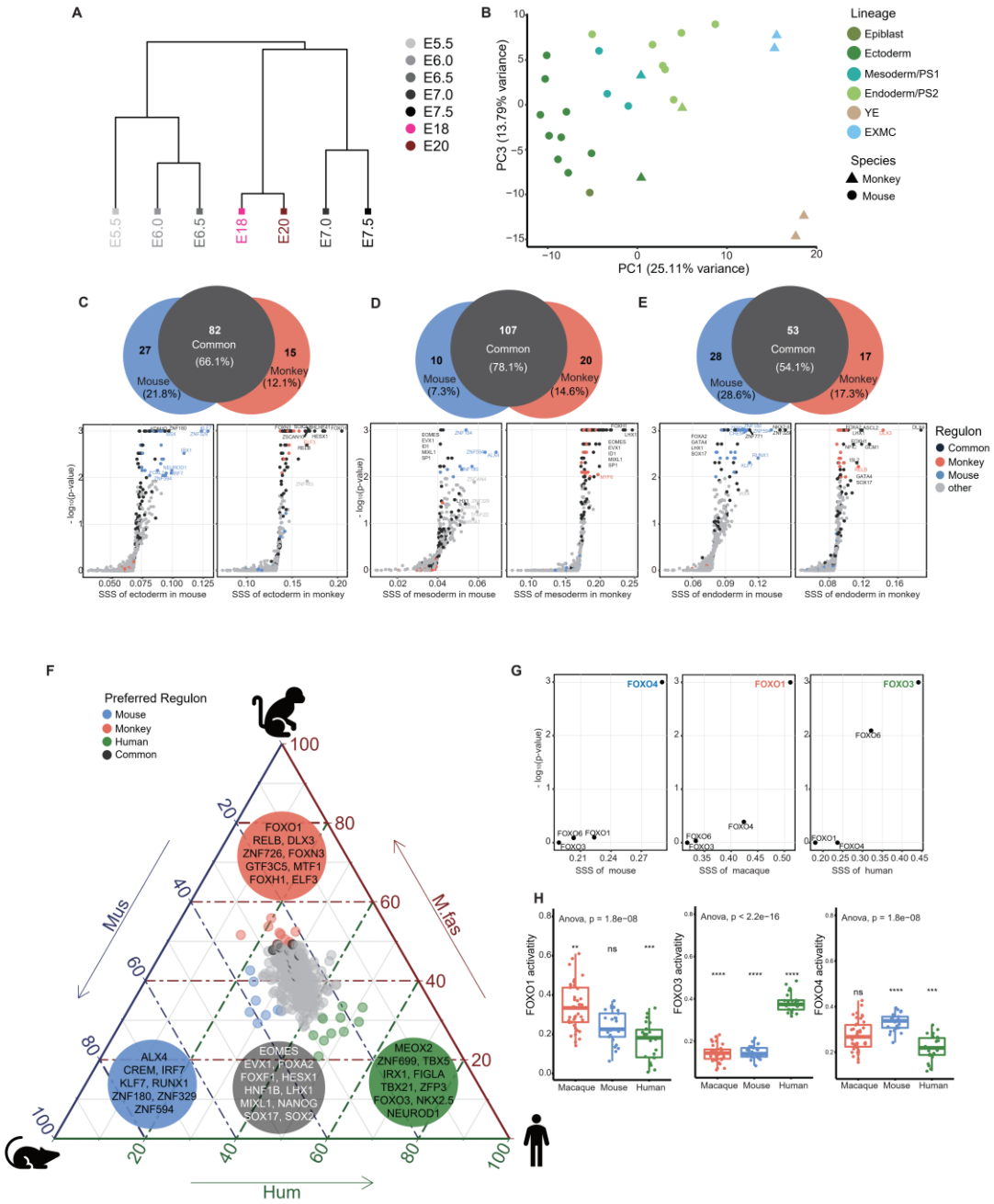

768

Figure 7 Cross-species spatial transcriptomic analysis reveals gastrulation developmental differences among mice, monkeys and humans

A, Hierarchical clustering analysis of mouse and monkey whole embryos in different gastrulation stages based on averaged dynamic regulons (n=451).

B, PCA analysis showing the lineage difference between mouse and monkey. YE, yolk-sac endoderm; EXMC, extra-embryonic mesenchyme tissues.

C-E, Species specific regulons between mouse and monkey in ectoderm, mesoderm and endoderm embryogenesis, respectively. Venn plot showed the lineage species specific and common regulons. The scatter plot showed the significant and specific regulons in different species germ layer. SSS, species/spatial domain-specificity score. Color code the specific type of regulons.

F, Ternary plot of the most divergent species-specific regulons in gastrulation between mouse, monkey and human. Top 10 regulons were colored and listed based on species - specificity score (SSS).

G. Species-specificity score of FOXO regulons between mouse, monkey and human gastrulation embryonic tissue.

H, The activities of FOXO regulons between mouse, monkey and human gastrulation embryonic tissue.

SUPPLEMENTAL INFORMATION

Supplemental Information includes Supplemental Experimental Procedures, eight figures, and three tables and can be found with this article online at ..

ACKNOWLEDGMENTS

We thank W. Ji for critical discussions, S.Suo for help of data analysis, and J. Xu, J.Zhang, M.Wang, L.Qin for experimental support. This work was supported in part by National Key R&D Program of China (2018YFA0801402, 2018YFA0107200, 2019YFA0801400), the "Strategic Priority Research Program" of the Chinese Academy of Sciences (XDA16020404 and XDA16010308), National Natural Science Foundation of China (31871456, 32100483), Guangdong Basic and Applied Basic Research Foundation (2019B151502054, 2019A1515110985).

AUTHOR CONTRIBUTIONS

N.J. and G.P. conceived the study. G.P., N.J. and W.S. supervised the project. G.P., N.J., W.S. and G.C. designed the experiments. G.C. and S.F. conducted the histology and IF and analyzed the data, G.C. and L.W. contributed to the 3D reconstruction of the histological sections, W.S., Y.Y., X.H., X.L., Y.D. and P.Z. performed samples collection, G.C. and G.P. performed the Geo-seq experiments and analyzed the spatial transcriptome data, K.T. and J.C. performed tissue staining, G.C., G.P., P.P.L.T. and N.J. wrote the paper with the help of all other authors.

DECLARATION OF INTERESTS

The authors declare no competing interests.

818 # STAR Methods

819 ## KEY RESOURCES TABLE

REAGENT or RESOURCE	SOURCE	IDENTIFIER
Antibodies		
OCT4	Santa Cruz Biotechnologies	Cat#sc-5279
GATA6	Cell Signaling Technology	Cat#5851
Brachyury /T	R&D Systems	Cat#AF2085
DAPI	Sigma-Aldrich	Cat#28718-90-3
Biotin-SP (long spacer) AffiniPure Donkey Anti-Goat IgG (H+L)	Jackson Immuno	Cat#705-065-147; RRID: AB_2340397
Biotin-SP (long spacer) AffiniPure Donkey Anti-Rabbit IgG (H+L)	Jackson Immuno	Cat#711-065-152; RRID: AB_2340593
Biotin-SP (long spacer) AffiniPure Donkey Anti-Mouse IgG (H+L)	Jackson Immuno	Cat#715-065-150; RRID: AB_2307438
Normal Donkey Serum	Jackson Immuno	Cat#017-000-121; RRID: AB_2337258
Chemicals, peptides, and recombinant proteins		
Tissue freezing medium (OCT)	Leica Microsystems	Cat#020108926
Cresyl violet acetate	Sigma-Aldrich	Cat#C5042
dNTP mix	Takara	Cat#4030
RiboLock RNase Inhibitor	Roche	Cat#Eo0382
SuperScript II reverse transcriptase	Invitrogen	Cat#18064-014
KAPA HiFi HotStart ReadyMix	KAPA Biosystems	Cat#KK2601
VAHTS DNA Clean Beads	Vazyme	Cat#N411-02
Betaine solution	Sigma-Aldrich	Cat#B0300-1VL
Guanidine isothiocyanate solution	Invitrogen	Cat#15577-018
Antigen retrieval solution	Dako	Cat#S169984
Fluoromount-G	SouthernBiotech	Cat#G1417-T937
Critical commercial assays		
Qubit dsDNA HS Assay Kit	Invitrogen	Cat#Q32854
TruePrep DNA library pre kit V2	Vazyme	Cat#TD502-02
Alexa Fluor™ 488 Tyramide SuperBoost™ Kit, streptavidin	Thermofisher	Cat#B40932
Deposited data		

Raw and processed Geo-seq data of gastrulating macaque	This paper	GEO: GSE182838
The single cell RNA-seq data of monkey gastrulating embryo (E13, E14, E16 and E17)	(Nakamura et al., 2016)	GEO: GSE74767
The spatiotemporal transcriptome of gastrulating mouse embryos	(Peng et al., 2019)	GEO: GSE120963
RNA-seq data of spatial sectioned human gastruloids	(Moris et al., 2020)	GEO: GSE123187
Single-cell transcriptome of human CS7 gastrula	(Tyser et al., 2021)	ArrayExpress: E-MTAB-9388
Experimental models: Organisms/strains		
Cynomolgus monkeys	Institute of Zoology and Kunming Institute of Zoology, Chinese Academy of Sciences (CAS)	N/A
Oligonucleotides		
3'CDS primer: AAGCAGTGGTATCAACGCAGAGTACTTTTTTTTTTTTTTTTTTTTTTTTTTTTTTTTVN	(Chen et al., 2017)	N/A
TSO primer: AAGCAGTGGTATCAACGCAGAGTACAT/rG//rG//iXNA_G/	(Chen et al., 2017)	N/A
IS PCR primer: AAGCAGTGGTATCAACGCAGAGT	(Chen et al., 2017)	N/A
mfGAPDH-qPCR-F: AACAGGGTGGTGGACCTCAT	(Nakamura et al., 2016)	N/A
mfGAPDH-qPCR-R: TTCCTCTTGTGCTCTCGCTG	(Nakamura et al., 2016)	N/A
mfGATA4-qPCR-F: TGGCTATAGCAGAGAATACCTTTGAACCA	(Nakamura et al., 2016)	N/A
mfGATA4-qPCR-R: ACAGGTTTGTGGGTTAGGGAGGGT	(Nakamura et al., 2016)	N/A
mfPOU5F1-qPCR-F: GGGAGGAGCTAGGGAAAGAGAACCTA	(Nakamura et al., 2016)	N/A

mfPOU5F1-qPCR-R: CCCCCACCCGTTGTGTTCCCA	(Nakamura et al., 2016)	N/A
Software and algorithms		
HISAT2	(Pertea et al., 2016)	http://daehwankimlab.github.io/hisat2/
R Studio	Rstudio	https://rstudio.com/products/rstudio/ download/
R	The R Foundation	https://cran.r-project.org/mirrors.html
Seurat	(Stuart et al., 2019)	https://satijalab.org/seurat/
SPOTlight	(Elosua-Bayes et al., 2021)	https://github.com/MarcElosua/SPOTlight
Vision	(DeTomaso et al., 2019)	www.github.com/YosefLab/VISION
Ucell	(Andreatta and Carmona, 2021)	https://github.com/carmonalab/UCell
SCENIC	(Aibar et al., 2017)	http://scenic.aertslab.org
WGCNA	(Langfelder and Horvath, 2008)	https://horvath.genetics.ucla.edu/html/CoexpressionNetwork/Rpackages/WGCNA/
Cellchat	(Jin et al., 2021)	https://github.com/sqjin/CellChat
Cytoscape (v.3.8.2)	(Otasek et al., 2019)	https://cytoscape.org/
Metascape	(Zhou et al., 2019)	http://metascape.org
clusterProfiler (version 3.12.0)	(Yu et al., 2012)	https://bioconductor.org/packages/release/bioc/html/clusterProfiler.html
TCseq	(Mengjun, 2019)	https://bioconductor.org/packages/release/bioc/html/TCseq.html
FIJI	(Schindelin et al., 2012)	https://imagej.net/Fiji
Vaa3D (version 3.5)	(Peng et al., 2010)	https://github.com/Vaa3D/release/releases/
Amira	Thermofisher	https://www.thermofisher.cn/cn/zh/home/electron-microscopy/products/software-em-3d-vis/amira-software.html
Other		
VS120	Olympus	N/A

BX51	Olympus	N/A

RESOURCE AVAILABILITY

Lead contact

Further information and requests for resources and reagents should be directed to and will be fulfilled by the Lead Contact, Guangdun Peng (peng_guangdun@gibh.ac.cn).

Materials availability

Unique materials generated in this study are available from the Lead Contact without restriction.

Data and code availability

The Cynomolgus monkey spatiotemporal RNA-seq raw and processed data have been deposited in the Gene Expression Omnibus database under accession number GSE182838 (the private token for reviewers: wxcncyssljgjlqj), and also can be downloaded from our website http://113.105.131.191:10010/Primate.Gastrulation/. Custom code and scripts are available from methods details and github (https://github.com/GuizhongCui/Primate.Gastrulation2021). All other data supporting the findings of this study are available from the corresponding author upon request.

EXPERIMENTAL MODEL AND SUBJECT DETAILS

All monkey experiment procedures were under the guidance of the Ethics

842 Committee of the Institute of Zoology and Kunming Institute of Zoology,
843 Chinese Academy of Sciences (CAS). The gastrulating embryos of
844 Cynomolgus monkeys (*Macaca fascicularis*) from natural conception and in
845 vitro fertilization (IVF) were both used in this study. The procedures in
846 Cynomolgus monkeys for oocyte collection, intra-cytoplasmic sperm injection,
847 pre-implantation embryo culture, and transfer of pre-implantation embryos into
848 foster mothers were performed as described previously (Niu et al., 2019;
849 Yamasaki et al., 2011). The day when the intra-cytoplasmic sperm injection was
850 performed was designated as embryonic day (E) 0. For the detection of
851 pregnancy of early post-implantation embryos, implanted embryos were
852 monitored by ultrasound scanning around E14 and the implanted uterus was
853 surgically removed and bisected for the isolation of embryos.
854 For naturally mated embryos, health adult female and male monkeys aged from
855 7-8 years were individually kept in an animal room with humidity at 40-70% and
856 temperature at 18-26 °C and exposed to a 12:12 light–dark cycle. The female
857 monkeys were observed at least two normal menstrual cycles confirmed by
858 virginal bleed before being allowed to mating with male monkeys. The first day
859 of bleeding was defined as day 1 of menses once menstrual cycle start. Then
860 venous blood was collected at 09:00 AM on menses days 7 to 18, and a male
861 monkey was allowed to mating with the female monkey. Blood serum was
862 separated by centrifugation and concentrations of E2 and P4 were assayed
863 using a chemiluminescent immunoassay. Once the peak of E2 was detected,
864 then the next day was defined as the day of ovulation and fertilization, and the
865 concentration of blood E2 and P4 were continuously measured. The pregnancy
866 was confirmed by the low level of E2, increased level of P4 and ultrasonography.
867

868 # METHOD DETAILS

869 **Monkey embryo H&E staining and immunofluorescent analysis**

870 Monkey post-implantation embryos by IVF procedure were harvested at
871 different stage from embryonic day 17(E17) to E21 every day (at least two
872 embryos in each stage), and whole embryos were fixed in 4%
873 paraformaldehyde (PFA) at 4°C overnight. The procedures of paraffin
874 embedding were carried out, and the embedding embryos were transversely
875 sectioned at a thickness of 5 μm. The sections were stained by H&E staining
876 and immunofluorescent staining as previously reported (Feng et al., 2017). In
877 brief, after dewaxed and rehydrated, the slides were stained in hematoxylin
878 solution for 30 sec and counterstained in eosin solution for 10 sec. For
879 immunofluorescence staining, the sections were incubated with primary
880 antibody in hybridization buffer overnight at 4 °C after blocked, and incubated
881 with secondary antibody for 1 hour (h) at room temperature. The sections were
882 counterstained with 4′,6′-diamidino-2-phenylindole (DAPI) and mounted with
883 mounting medium. Bright field images and fluorescent images were collected
884 on an Olympus VS120 and Olympus BX51 microscope respectively, and
885 aligned manually using Adobe Photoshop CC.

886 **Determination of gastrulation cell number and mitotic activity**

887 The number of cells contained in epiblast/ectoderm, mesoderm and
888 hypoblast/endoderm were determined by counting nuclei on every section of
889 the gastrulating embryos. The total score was then adjusted by applying
890 Abercrombie's correction formula (Abercrombie, 1946) to give an estimate of
891 the actual cell number. In detail, the average number of cells per section (*P*):

892 $$P = A\frac{M}{L + M}$$

893 *A* is the crude count of number of nuclei fragments, *M* is the thickness of the
894 section (*M*=5μm in this study), and L the average length of the nuclei (*L*=10μm
895 in this work).
896 Cell cycle times can be calculated from the equation (Snow, 1977), C_t means
897 the cell number at *t* stage:

898 $$T = \frac{\Delta t}{C_{t+1}/C_t}$$

899

900 **3D reconstructions of gastrulating monkey embryos**

901 The Vaa3D (version 3.5) and Amira (version 6.0.1) were used for the 3D
902 reconstruction process, consisting of alignment, segmentation and visualization
903 (de Bakker et al., 2016; Peng et al., 2010). In brief, grey scale processing was
904 performed by Photoshop CC (Adobe Systems), and alignment of the stitched
905 serial images was mainly implemented by manual after automatically
906 adjustments. The aligned 3D images were segmented into epiblast/ectoderm,
907 primitive streak, hypoblast/endoderm and mesoderm. Then, triangulated
908 surface files were made using the *SurfaceGen* function, and triangle reduction
909 (*Simplify*) and surface smoothing (*SmoothSurface*) were also applied for
910 visualization. Besides, the Vaa3D was also applied to aligned sections to
911 visualize the 3D structure of specific tissues.

912 **Spatial molecular profiling of monkey embryos**

913 The spatial transcriptome of gastrulating embryos was obtained according to
914 Geo-seq protocol with minor modifications (Peng et al., 2019). Briefly, whole
915 embryos (two monkey embryos at E18 and one at E20 from natural conception)
916 were embedded in OCT (Leica Microsystems, catalogue no. 020108926), and
917 cryo-sectioned in the coronal plane serially from the anterior region to the

918 posterior region at a thickness of 20 μm. Sections were transferred onto LCM
919 PEN membrane slides, fixed immediately by ethanol and stained with 1% cresyl
920 violet acetate in 75% ethanol solution (Sigma-Aldrich). The embryonic tissue
921 was divided into upper, middle and lower layer, and the extraembryonic tissue
922 was divided into extra-embryonic mesenchyme 1/2 and yolk-sac endoderm 1/2
923 based on the good morphology sections. Populations of 5-50 cells were
924 collected by laser microdissection, and total RNA pellets were dissolved in lysis
925 solution, followed by reverse transcription using SuperScript II reverse
926 transcriptase (Invitrogen), whole transcription amplification with KAPA HiFi
927 HotStart ReadyMix (2X; KAPA Biosystems). The PCR product of LCM samples
928 were used for automated single-cell RNA-Seq library construction based on the
929 Bravo robot station(Cui et al., 2019). In brief, PCR product were purified using
930 0.75X AMPure XP beads (Agencourt), quantified with Qubit dsDNA HS Assay
931 Kit (Thermo Fisher) on Envision (PerkinElmer), and cDNA library was
932 constructed by DNA Library Prep Kit V2 for Illumina (Vazyme) and sequenced
933 on an Illumina Nova 6000 instrument using a 150 bp paired-end-reads setting.

934 QUANTIFICATION AND STATISTICAL ANALYSIS

935 Processing of RNA-seq data

936 Sequencing quality of raw sequencing data was evaluated by fastp (Chen et al.,
937 2018). The genome sequence Macaca_fascicularis_5.0 for Cynomolgus
938 monkeys (*Macaca fascicularis*) were obtained from the Ensemble
939 (https://asia.ensembl.org/index.html). Reads were mapped to the
940 Macaca_fascicularis_5.0 genome assemblies by HISAT2 (Pertea et al., 2016)
941 using default settings. Mapping ratio was calculated based on the number of
942 mapped reads and total reads for each sample. All mapped reads were
943 processed by StringTie(Pertea et al., 2016) to quantify gene expression levels

944 (measured by TPM and FPKM, Transcripts Per Kilobase per Million mapped
945 reads and Fragment Per Kilobase per Million mapped reads respectively) using
946 default parameters. Seurat package (version 3.1.5) (Stuart et al., 2019) was
947 applied to dimensionality reduction analysis in R (version 4.0.3). Gene
948 expressed in at least two samples across all samples were selected for further
949 analysis. After filtering, data in each sample were normalized, the 5,000 most
950 variable genes were identified with *vst* method, and the expression levels of
951 these genes were scaled before performing Principal Component Analysis
952 (PCA) in variable gene space. Next, 5 principal components were used for
953 graph-based clustering (resolution = 2) and UMAP dimensionality reduction
954 was computed using *RunUMAP* function with default parameters. The
955 Spearman correlation coefficient (SCC) of spatial domain between embryonic
956 replicates or developmental stages were calculated based on average
957 expression of all gene.
958

959 **Identification of differentially expressed genes (DEGs) and clustering**
960 **analysis**

961 Gene expression levels for each sample were $\log_2$ (TPM+1) transformed and
962 then combined 5,000 most variable genes with top 150 highest and lowest
963 Principal Component (PC) loading genes (by using *FactorMineR* in R) from
964 PC1-5 to identify the DEGs. In total, 1,305 genes were identified as DEGs.
965 Finally, unsupervised hierarchical clustering was performed using the *hclust*
966 function Ward's method (ward.D2) to determine the final spatial domains of
967 embryonic and extraembryonic tissues based on the expression profile of DEGs.
968

969 **Integrating scRNA-seq and spatial transcriptome**

970 To investigate the architecture of the cell-type distribution in spatial
971 transcriptome, we integrate both single-cell and spatial transcriptomics data of
972 monkey gastrulating embryo *in vivo* to infer the spatial locations of different cell
973 types in a tissue. The single cell RNA-seq data of monkey gastrulating embryo
974 (E13, E14, E16 and E17) from GSE74767(Nakamura et al., 2016), and apply
975 *FindAllMarkers* function of Seurat pipeline to identify cluster markers.
976 SPOTlight, a deconvolution algorithm that built upon a non-negative matrix
977 factorization (NMF) regression algorithm was used for cell-type deconvolution
978 in spatial transcriptome (Elosua-Bayes et al., 2021). In brief, SPOTlight
979 factorizes the normalized scRNA-seq gene expression matrix into two lower
980 dimensionality matrices using NMF, and cell-level topic distribution matrix is
981 used to learn the cell-type specific topic profiles through a Non-Negative Least
982 Squares regression (NNLS). The weights of each cell-type specific topic profile
983 represent the cell-type proportions across all samples in spatial transcriptome.
984 Furthermore, we used the averages of single-cell detectable gene expression
985 in the same annotated cell type and spatial samples at the same location to
986 calculate the SCC.
987

988 **Pathway activity analysis and epithelial-mesenchymal transition scores**
989 **analysis**

990 To identify the key biological properties of spatial samples, Vision (DeTomaso
991 et al., 2019; Zhang et al., 2020) and Ucell (Andreatta and Carmona, 2021) were
992 applied to perform functional enrichment analyses. The homologous target
993 genes of WNT, BMP, FGF, NODAL and Hippo/Yap signaling pathways between
994 monkey and mouse gastrulating (Peng et al., 2019) were used as signatures of

995 *vision* analysis. In addition, we input the gene signatures of MSigDB, which
996 curated by the Broad institute, to explore the transcriptional effects of regions.
997 To evaluate the epithelial–mesenchymal transition (EMT) of epiblast cells,
998 scoring EMT based on the Mann-Whitney U statistic (Andreatta and Carmona,
999 2021). The EMT-inducing transcriptions factors (EMT-TFs) zinc-finger E-box-
1000 binding family (ZEB1 and ZEB2), basic helix–loop–helix transcription factors
1001 (TWIST1 and TWIST2) and snail family transcriptional repressor (SNAI1 and
1002 SNAI2) were included as signature of mesenchymal state. The markers
1003 associated with the mesenchymal state vimentin (VIM), fibronectin and β1 (FN1)
1004 and matrix metalloproteinase (MMP2) and the markers related to the epithelial
1005 state E-cadherin (CDH1), grainyhead like transcription factor (GRHL2),
1006 epithelial cell adhesion molecule (EPCAM), Occludins (OCLN), Claudins
1007 (CLDN4 and CLDN7) and cytokeratins (KRT19) were also add into Ucell
1008 analysis (Chakraborty et al., 2020; Dongre and Weinberg, 2019; Lamouille et
1009 al., 2014). The EMT score is the difference of epithelial score minus
1010 mesenchymal score (E-M), and the higher EMT scores, the more epidermal-
1011 like state.

1012 **Reconstruction of regulons in embryonic and extraembryonic tissues**

1013 For inferring Cynomolgus monkey's gene regulatory network (GRN) using
1014 SCENIC (Aibar et al., 2017), common genes listed in the Cynomolgus
1015 monkeys–humans one-to-one annotation table were used(Nakamura et al.,
1016 2016). 17,019 common genes were first filtered to exclude all genes detected
1017 in fewer than two samples, and then were used to identified TF-gene co-
1018 expression modules. Subsequently, those modules are refined via RcisTarget
1019 by keeping only those genes than contain the respective transcription factor
1020 binding motif. Finally, SCENIC found 323 regulons in monkey gastrulating
1021 embryos, whose regulatory activities were represented by AUCell values. To

1022 identify regulons associated with spatial domains of gastrulating monkey
1023 embryos, we used the regulon activity score for each sample to perform PCA,
1024 heatmap display and network analysis (Peng et al., 2016; Peng et al., 2019).
1025 Regulons shared in 250 most variable regulons and top 100 highest and lowest
1026 PC loading regulons from PC1-3 were defined as specific regulons. For network
1027 visualization, the regulon was assigned to the tissue with highest average
1028 regulon activity score. The SCC was calculated in the same lineage, and the
1029 absolute value was greater than 0.95 for further analysis. The edge weights
1030 were proportional to the SCC values of two correlated nodes.

1031 **Co-expression gene network and interaction analysis**

1032 To identify biologically relevant patterns of spatial samples, we performed
1033 weighted gene co-expression network analysis using R package WGCNA
1034 (Langfelder and Horvath, 2008). Briefly, a soft power threshold of 10 was set to
1035 constructed unsigned network and the minimum module size was set to 10
1036 genes. Eight gene modules with significant correlation in the seven spatial cell
1037 populations were used to draw gene modules for each cell type. Only top 30
1038 genes with highest 100 correlation coefficient values in each module were kept
1039 when visualizing the modules with Cytoscape (v.3.8.2)(Otasek et al., 2019).
1040 To quantitatively infer and analyze intercellular communication networks,
1041 Cellchat was applied to predict potential interaction probability scores (Jin et al.,
1042 2021). Human gene names were converted to Cynomolgus monkey genes
1043 using orthology data from monkeys–humans one-to-one annotation table, with
1044 17,542 genes in common between the two species (Nakamura et al., 2016).
1045 We use the tissue type of spatial sample based on regulon activity clustering
1046 as label information, and calculated an aggregated interaction probability by
1047 Cellchat based on the expression level of ligand–receptor pairs.

1048 **Functional enrichment analysis and phenotype analysis**

1049 We applied Metascape (Zhou et al., 2019) (http://metascape.org), KOBAS-i
1050 (KOBAS intelligent version, version 3.0) (Bu et al., 2021) and R package
1051 clusterProfiler (version 3.12.0) (Yu et al., 2012) to perform Gene Ontology and
1052 pathways enrichment analysis for each group of DEGs and regulon TFs. The
1053 TFs which display strong gastrulation phenotypes from Mouse Genome
1054 Information (MGI) database were highlighted and visualized in the regulon
1055 network.
1056

1057 **Cross-species comparative analysis**

1058 The spatiotemporal transcriptome of gastrulating mouse embryos was
1059 generated in our previous work (Peng et al., 2019) (GSE120963), and used the
1060 RNA-seq data of spatial sectioned human gastruloids (Moris et al., 2020)
1061 (GSE123187) and single cell transcriptome (E-MTAB-9388) to assess human
1062 gastrulating embryos. For comparison of the gene expression among mouse,
1063 Cynomolgus monkeys and human, ortholog genes of these three species from
1064 Ensemble were used for further analysis (Nakamura et al., 2016). To reveal the
1065 temporal pattern of time course sequencing data, the TCseq package (Mengjun,
1066 2019) was performed to classify the dynamic regulons into various types of
1067 clusters, with the genes in each cluster were then processed for functional
1068 enrichment analysis. Then the total of 451 different regulons across five stages
1069 of gastrulation were used for hierarchical clustering and PCA analysis.
1070 To quantify the species germ layer specificity of a regulon, an entropy-based
1071 strategy was modified from regulon specificity score (RSS) (Peng et al., 2019;
1072 Suo et al., 2018). All 490 regulon gene lists which calculated by SCENIC in
1073 monkey gastrulating embryos were reanalyzed in natural logarithms

transformed expressed matrix of three species by AUCell package (version 1.16.0). Then the Jensen–Shannon divergence (JSD) algorithm was used to identify species-spatial domain-specific regulons by philentropy package (version 0.5.0) (Drost, 2018). Finally, for distribution of each regulon P_1 and predefined pattern P_2, the species/spatial domain- specificity score (*SSS*) between P_1 and P_2 was defined by converting JSD to a similarity score:

$$SSS = 1 - \sqrt{JSD(P_1, P_2)}$$

To evaluate the significance of regulon specificity in each species spatial domain, the regulon-activity score was permuted across all samples 1,000 times, then calculated *SSS*, and finally a permutation *p* value was calculated as the number of times that $SSS_{\text{permutation}} > SSS_{\text{true}}$ divided by 1,000. Only the significant regulons ($P < 0.01$), which were specifically activated in species-spatial domains, were kept for downstream analysis. Ternary plot was applied to show the proportion of *SSS* mice, monkeys and humans.

SUPPLEMENTAL INFORMATION

Figure S1

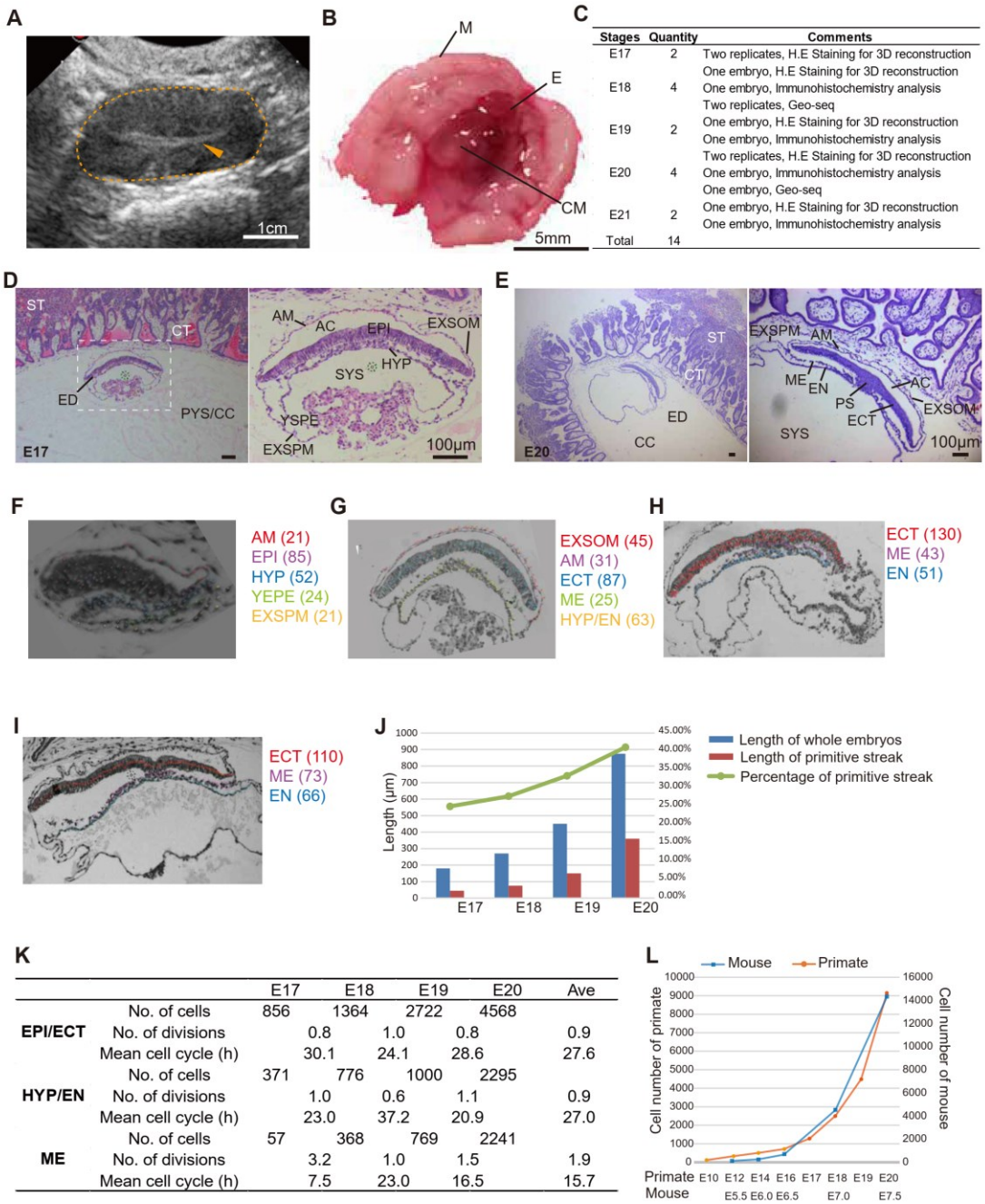

Stages	Quantity	Comments
E17	2	Two replicates, H.E Staining for 3D reconstruction
E18	4	One embryo, H.E Staining for 3D reconstruction One embryo, Immunohistochemistry analysis Two replicates, Geo-seq
E19	2	One embryo, H.E Staining for 3D reconstruction One embryo, Immunohistochemistry analysis
E20	4	Two replicates, H.E Staining for 3D reconstruction One embryo, Immunohistochemistry analysis One embryo, Geo-seq
E21	2	One embryo, H.E Staining for 3D reconstruction One embryo, Immunohistochemistry analysis
Total	14	

K

		E17	E18	E19	E20	Ave
EPI/ECT	No. of cells	856	1364	2722	4568	
	No. of divisions	0.8	1.0	0.8		0.9
	Mean cell cycle (h)	30.1	24.1	28.6		27.6
HYP/EN	No. of cells	371	776	1000	2295	
	No. of divisions	1.0	0.6	1.1		0.9
	Mean cell cycle (h)	23.0	37.2	20.9		27.0
ME	No. of cells	57	368	769	2241	
	No. of divisions	3.2	1.0	1.5		1.9
	Mean cell cycle (h)	7.5	23.0	16.5		15.7

1094 **Figure S1 Macaque gastrulating embryos.**

1095 A, Ultrasound diagnosis of the monkey's recipient uterus for the implantation of
1096 transplanted embryos at E17. Dashed circles indicate the uterus and
1097 arrowheads indicate the chorionic cavity. Scale bars, 1 centimeter.
1098 B, Images of dissected monkey uterus at gastrulation stage. M, myometrium;
1099 E, endometrium; CM, chorionic membranes. Scale bars, 5 millimeters.
1100 C, Summary of collected embryos during gastrulation.
1101 D, Haematoxylin and eosin staining of the section of replicate embryo at E17.
1102 The image at right is a higher magnification of the area boxed on the left. ST,
1103 syncytiotrophoblast; CT, cytotrophoblast; PYS, primary yolk sac; CC, chorionic
1104 cavity; ED, Embryonic disc; AC, amniotic cavity; AM, Amnion; EPI, epiblast;
1105 HYP, hypoblast; YSPE, yolk-sac parietal endoderm; EXSPM, extraembryonic
1106 splanchnic mesoderm; EXSOM, extraembryonic somatic mesoderm; SYS,
1107 secondary yolk sac. Scale bar, 100μm
1108 E, Haematoxylin and eosin staining of the section of replicate embryo at E20.
1109 The left is the lower magnification images. Scale bar, 100μm
1110 F-I, The number of nuclei fragments contained in epiblast/ectoderm, mesoderm
1111 and hypoblast/endoderm were counted on every section of the E17 (F), E18
1112 (G), E19 (H) and E20 (I) embryos. AM, Amnion; EPI, epiblast; ECT, ectoderm;
1113 ME, mesoderm; HYP, hypoblast; EN, endoderm; YSPE, yolk-sac parietal
1114 endoderm; EXSPM, extraembryonic splanchnic mesoderm; EXSOM,
1115 extraembryonic somatic mesoderm.
1116 J, The percentage of length of primitive streak. The length of embryo was
1117 assessed by total sections, while using sections with gastrulation area to
1118 evaluate the length of primitive streak.
1119 K, Cell numbers and mitotic activity of germ layers of gastrulating monkey
1120 embryos. EPI, epiblast; ECT, ectoderm; ME, mesoderm; HYP, hypoblast; EN,
1121 endoderm.

1122 L. Cell numbers of gastrulation in mouse and primate embryos. The cell number
1123 of primate embryos before E16 were got from in vitro cultured human embryos
1124 (Xiang et al., 2019), and the cell number of primate embryos during gastrulation
1125 were estimated by histological analysis. The cell number of mouse embryos
1126 were adapted from histological determination (Snow, 1977).
1127

1128 Figure S2

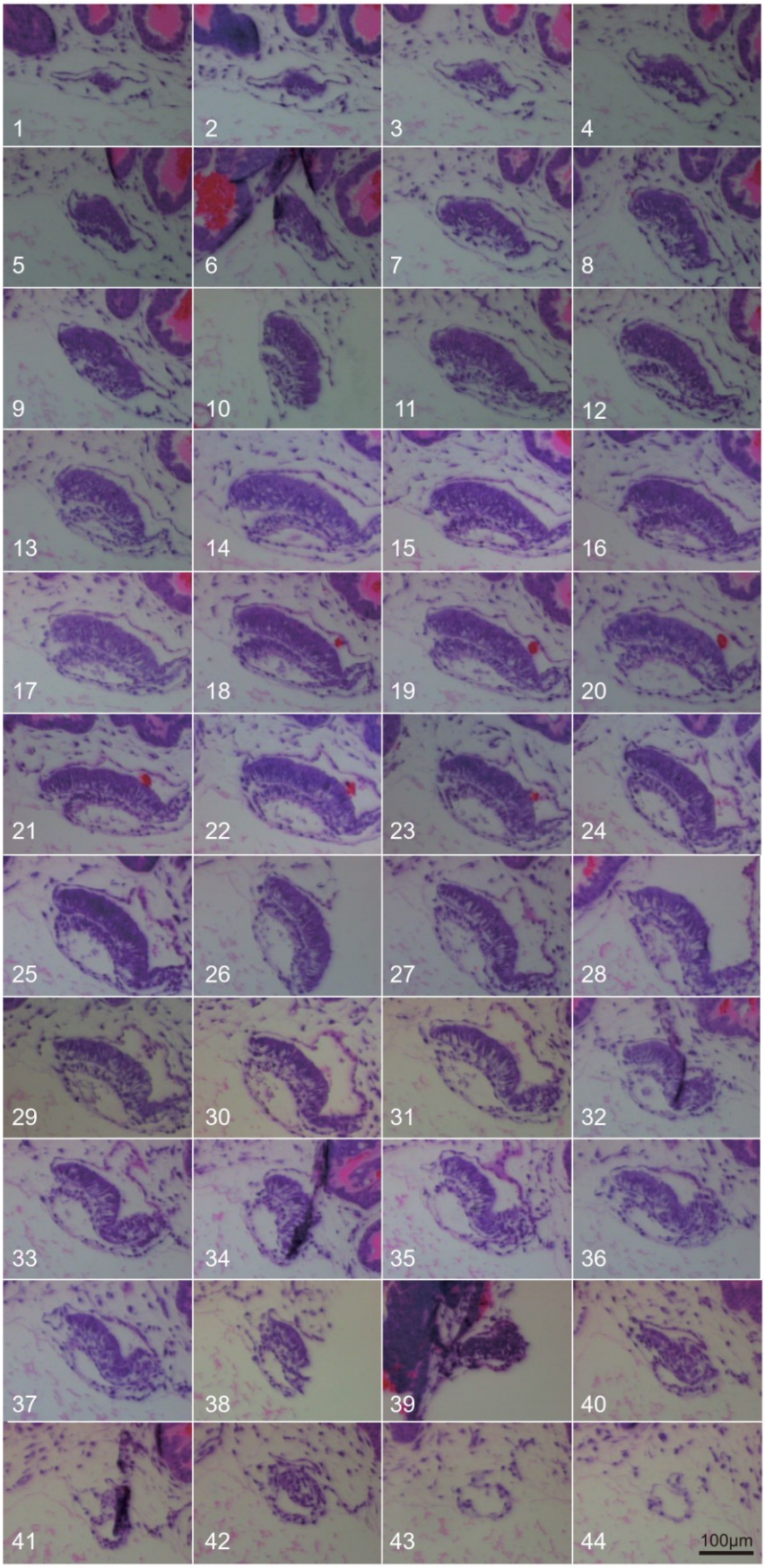

1129

1130 **Figure S2 Histology of serial section of E17 monkey embryo.**

1131 Haematoxylin and eosin staining of the serial sections of gastrulation embryo
1132 at E17. Scale bar, 100μm
1133

1134 Figure S3

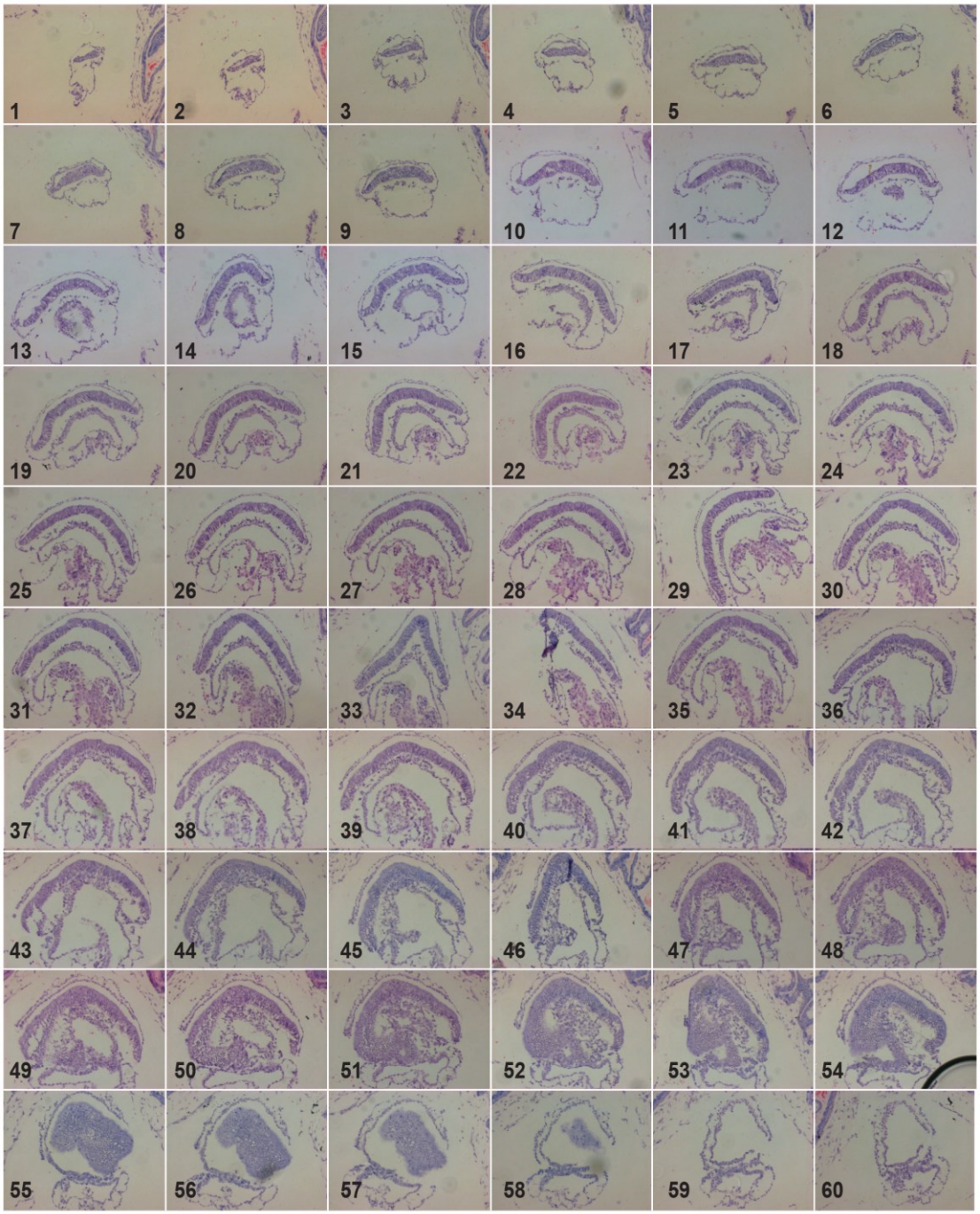

1135

1136 **Figure S3 Histology of serial section of E18 monkey embryo.**

1137 Haematoxylin and eosin staining of the serial sections of gastrulation embryo

1138 at E18. Scale bar, 100μm

1139

Figure S4-PART1

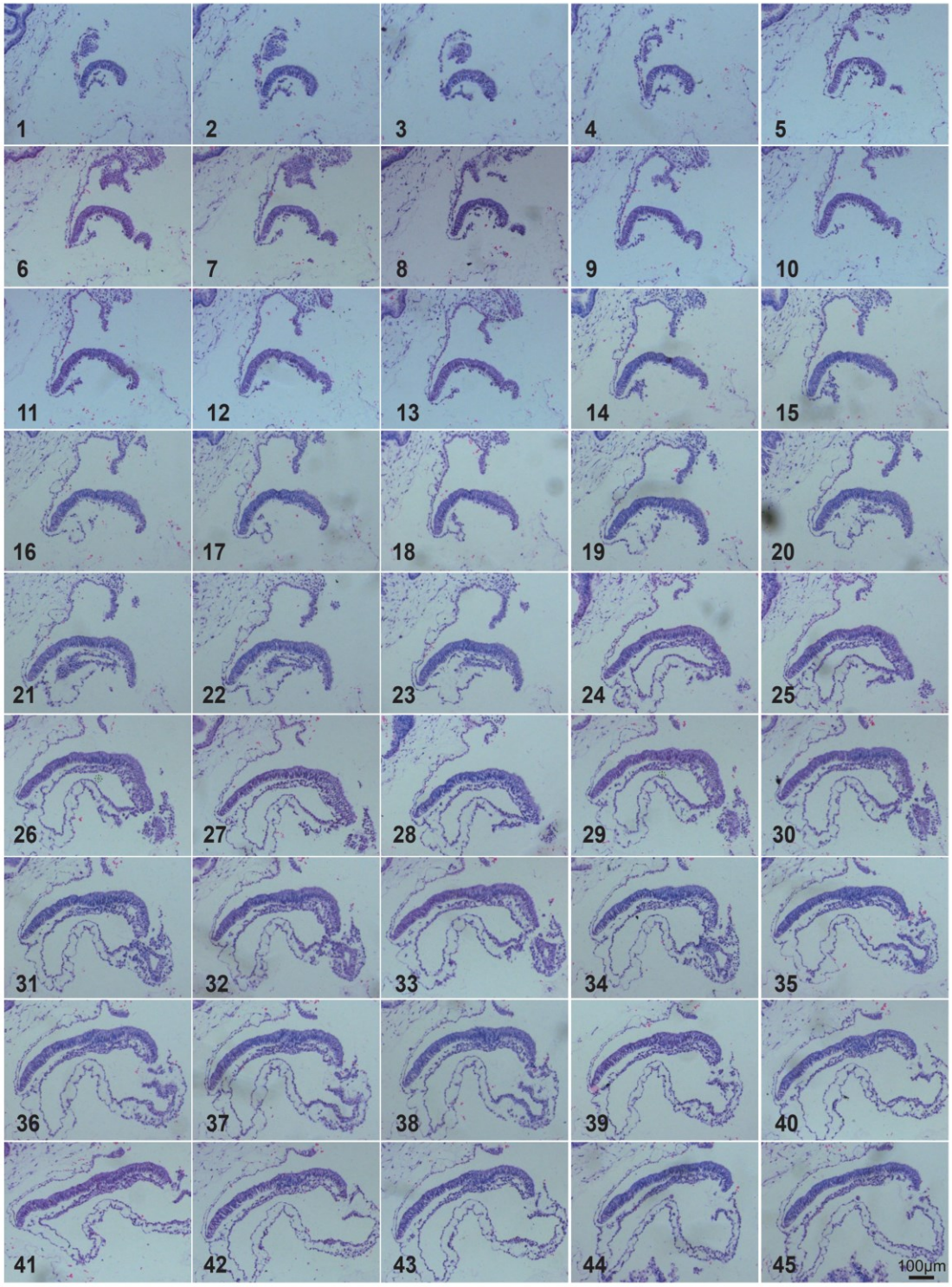

1143 Figure S4-PART2

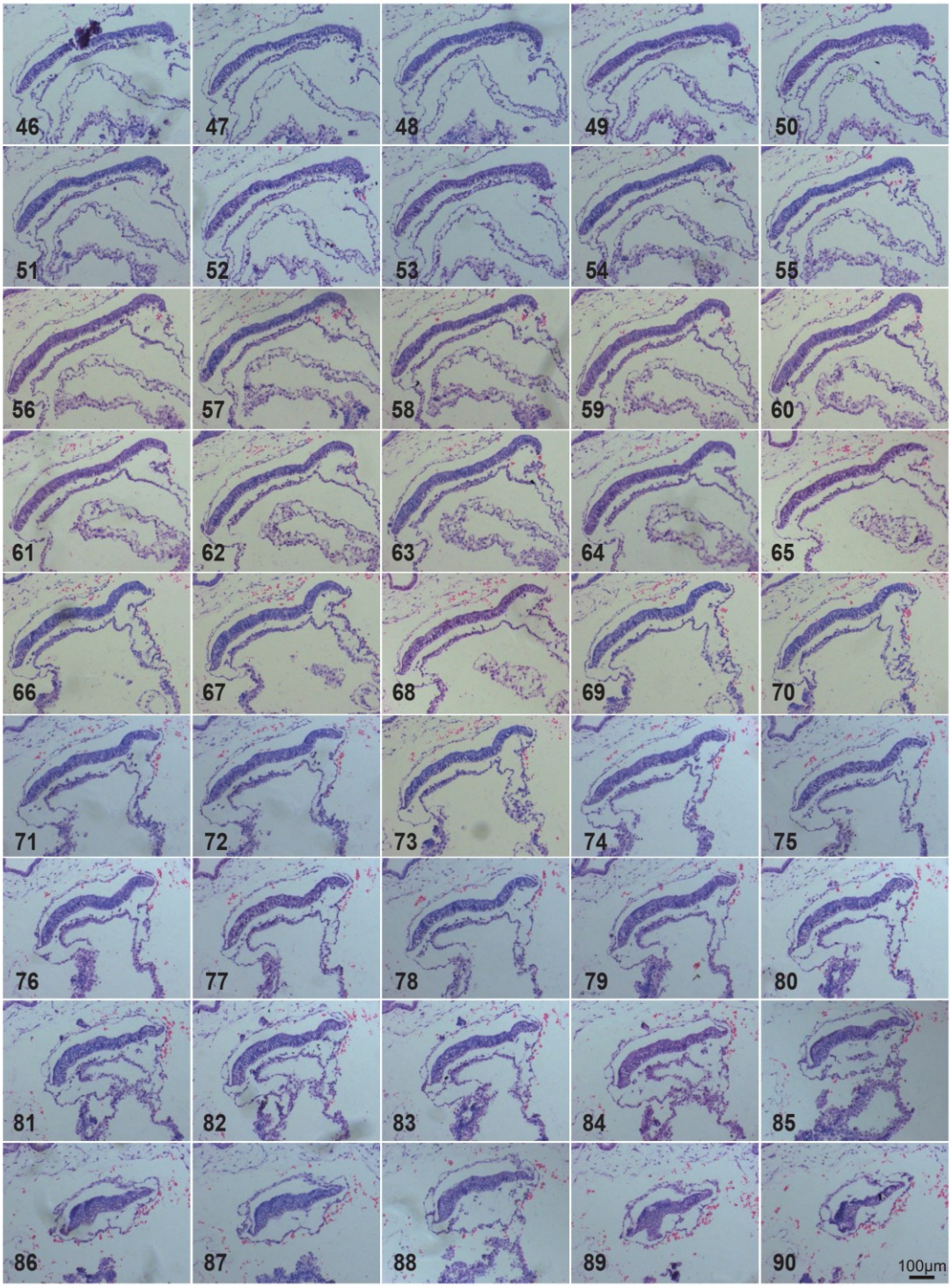

1144

1145 **Figure S4 Histology of serial section of E19 monkey embryo.**

1146 Haematoxylin and eosin staining of the serial sections of gastrulation embryo

1147 at E19. Scale bar, 100μm

Figure S5-PART1

Figure S5-PART2

1154 Figure S5-PART3

1155

1156 **Figure S5 Histology of serial section of E20 monkey embryo.**

1157 Haematoxylin and eosin staining of the serial sections of gastrulation embryo

1158 at E20. Scale bar, 100μm

1159

Figure S6-PART1

1163 Figure S6-PART2

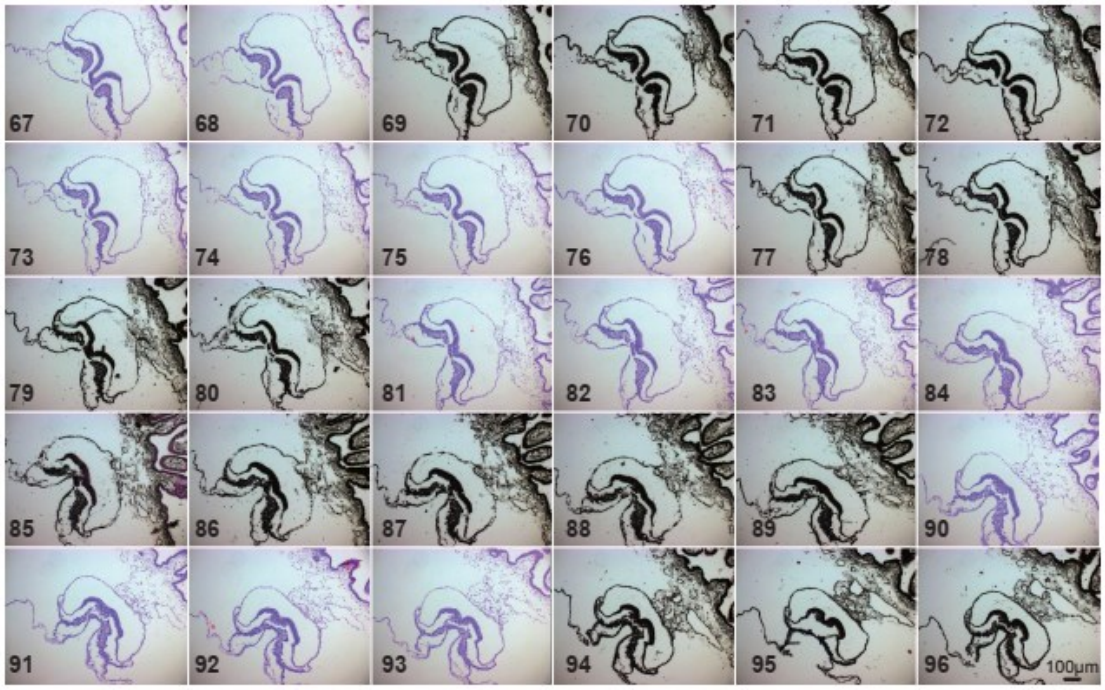

1164

1165 **Figure S6 Histology of serial section of E21 monkey embryo.**

1166 Haematoxylin and eosin staining of the serial sections of gastrulation embryo

1167 at E21. Scale bar, 100μm

1168

Figure S7

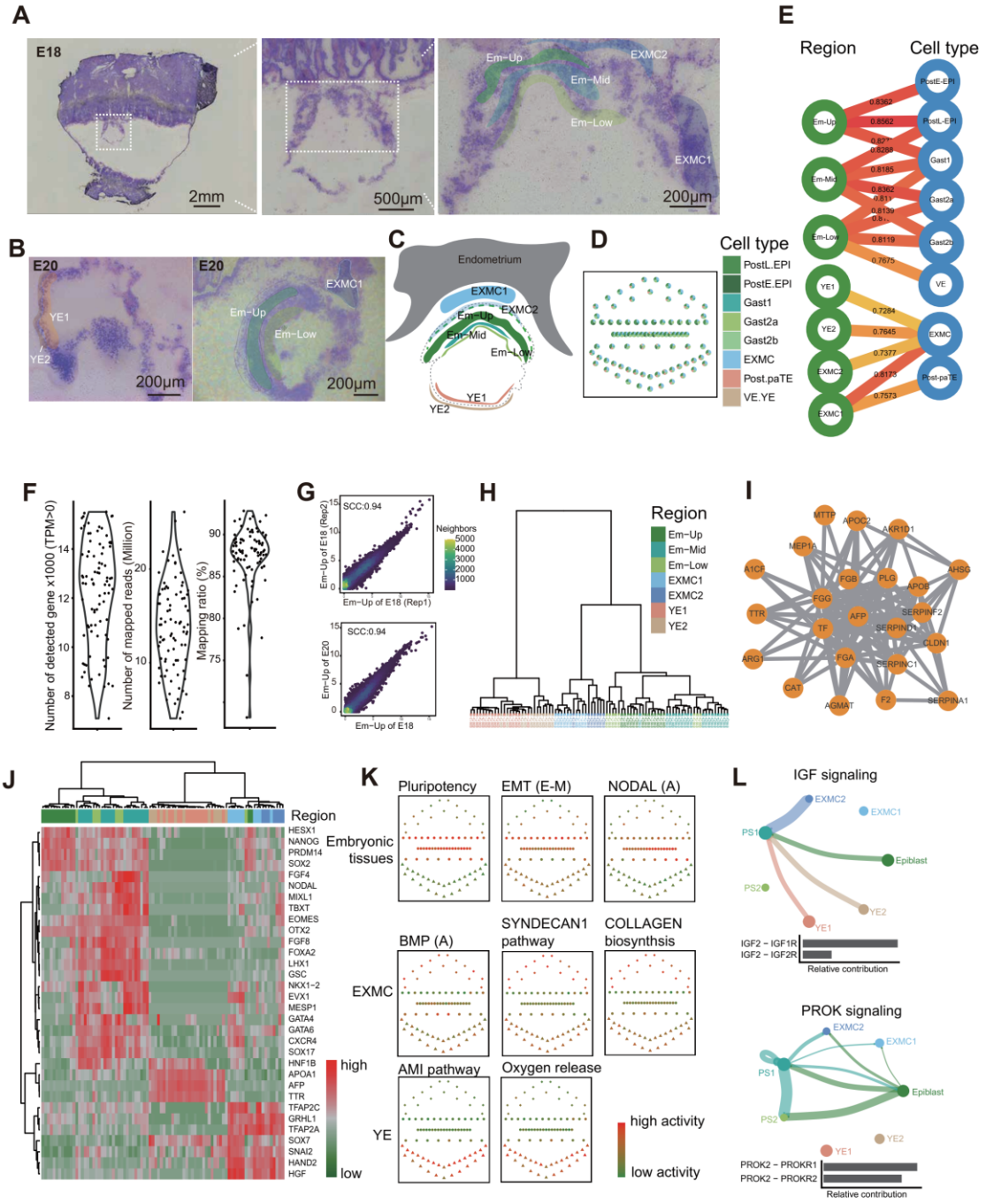
A
E18
2mm
500μm
200μm
Em-Up
EXMC2
Em-Mid
Em-Low
EXMC1
B
E20
YE1
YE2
200μm
C
Endometrium
D
Cell type
PostL.EPI
PostE.EPI
Gast1
Gast2a
Gast2b
EXMC
Post.paTE
VE.YE
E
Region
Cell type
F
Number of detected gene x1000 (TPM>0)
Number of mapped reads (Million)
Mapping ratio (%)
G
SCC:0.94
Neighbors
Em-Up of E18 (Rep2)
Em-Up of E18 (Rep1)
Em-Up of E20
Em-Up of E18
H
Region
Em-Up
Em-Mid
Em-Low
EXMC1
EXMC2
YE1
YE2
I
J
Region
HESX1
NANOG
PRDM14
SOX2
FGF4
NODAL
MIXL1
TBXT
EOMES
OTX2
FGF8
FOXA2
LHX1
GSC
NKX1-2
EVX1
MESP1
GATA4
GATA6
CXCR4
SOX17
HNF1B
APOA1
AFP
TTR
TFAP2C
GRHL1
TFAP2A
SOX7
SNAI2
HAND2
HGF
high
low
K
Pluripotency
EMT (E-M)
NODAL (A)
Embryonic tissues
BMP (A)
SYNDECAN1 pathway
COLLAGEN biosynthsis
EXMC
AMI pathway
Oxygen release
YE
high activity
low activity
L
IGF signaling
EXMC2
EXMC1
PS1
Epiblast
PS2
YE2
YE1
IGF2 - IGF1R
IGF2 - IGF2R
Relative contribution
PROK signaling
PROK2 - PROKR1
PROK2 - PROKR2

1172 **Figure S7 Spatial transcriptome analysis of monkey embryos at E18 and**
1173 **E20 by Geo-seq**

1174 A-C. Embryonic and extraembryonic tissues were captured by laser
1175 microdissection at E18 (A) and E20 (B). Representative sampling locations in
1176 7 different regions were shaded respectively. The schematic diagram showed
1177 the collected tissue regions (C). Em-Up, upper layer of embryonic tissue; Em-
1178 Mid, middle layer of embryonic tissue; Em-Low, lower layer of embryonic tissue;
1179 EXMC1/2, part of extra-embryonic mesenchyme tissues; YE1/2, part of yolk-
1180 sac endoderm.
1181 D. Cell-type deconvolution in spatial transcriptomics samples. The single cell
1182 RNA-seq data of monkey gastrulating embryos was download from previous
1183 work GSE74767 (Nakamura et al., 2016), and the STGE-plot represents the
1184 spatial sampling in monkey embryos. The colour coding is as indicated.
1185 E. The Spearman correlation coefficient of cell population between spatial (red
1186 module) and single cell annotated cell types (blue module, download from
1187 GSE74767 (Nakamura et al., 2016)) showing the location of specific cell. The
1188 color coding is spearman correlation coefficient (SCC).
1189 F. Violin plot showing the number of detected genes (TPM > 0), number of
1190 mapped reads (Million) and mapping ratio of samples (n=86).
1191 G. The Spearman correlation coefficient (SCC) of spatial domain. Upper panel
1192 showed the SCC between embryonic replicates at E18, and lower panel
1193 presented the SCC between developmental stages. The colorbar represent the
1194 density of gene number.
1195 H. Hierarchical clustering analysis for the embryonic and extraembryonic
1196 tissues of monkey embryo based on the expression level of DEGs. Color code
1197 the different sectors.
1198 I. Weighted gene co-expression network analysis (WGCNA) represented as

highest correlation coefficient values for yolk sac endoderm.

J. Heatmap showing the expression pattern of germ-layer marker genes. Top colored bars indicate the sample regions as F.

K. Pathway activity and epithelial-mesenchymal transition (EMT) scores analysis of the embryonic, extra-embryonic mesenchyme and yolk-sac endoderm tissues. The higher EMT scores (E-M), the more epidermal-like state. The colour coding is as indicated.

L. The inferred IGF and PROK signaling networks and relative contribution of each ligand-receptor pair to those overall signaling networks. Circle sizes are proportional to the number of cells in each cell group and edge width represents the communication probability.

Figure S8

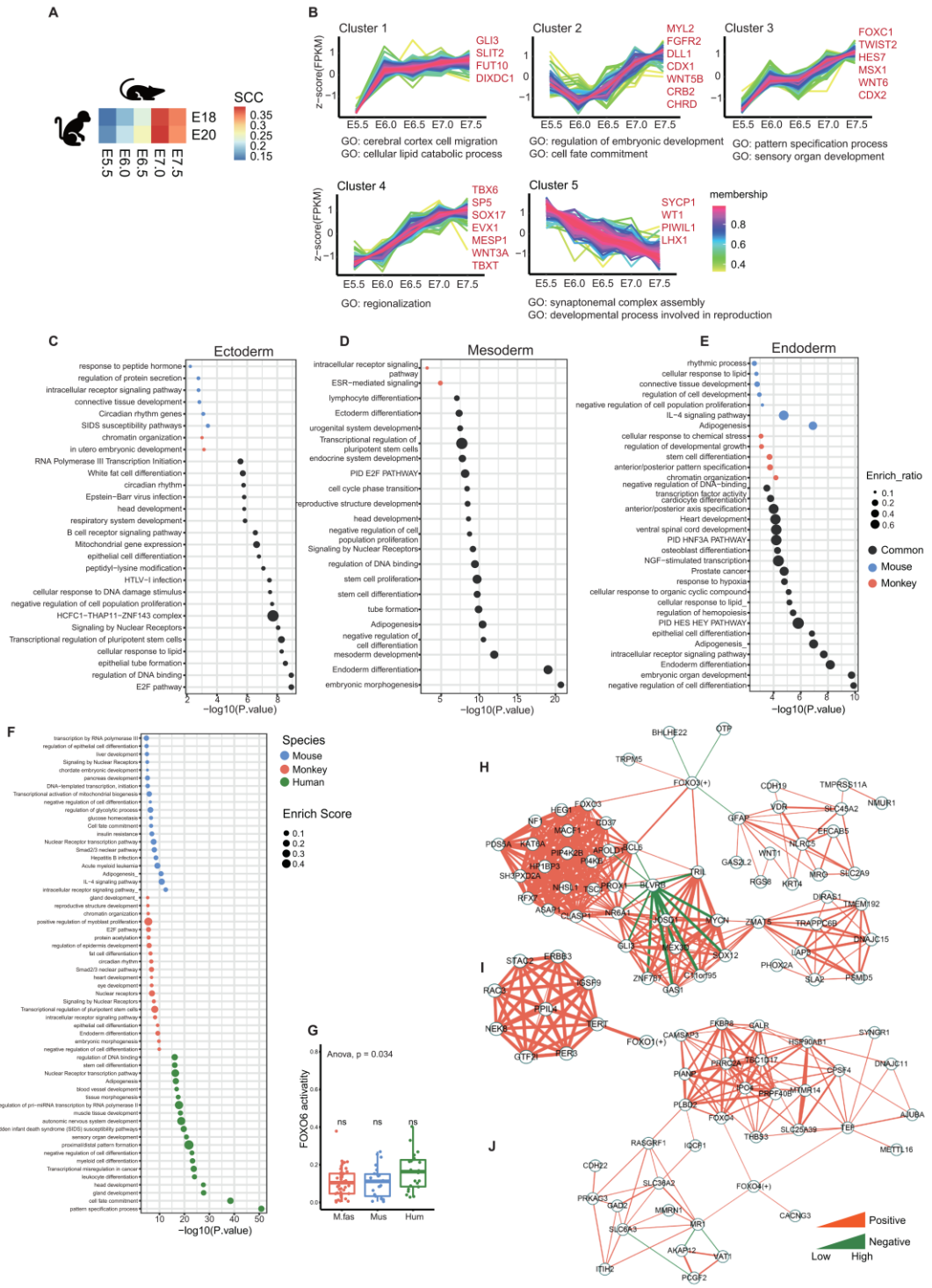
A
SCC
E18
E20
E5.5
E6.0
E6.5
E7.0
E7.5
B
Cluster 1
GLI3
SLIT2
FUT10
DIXDC1
GO: cerebral cortex cell migration
GO: cellular lipid catabolic process
Cluster 2
MYL2
FGFR2
DLL1
CDX1
WNT5B
CRB2
CHRD
GO: regulation of embryonic development
GO: cell fate commitment
Cluster 3
FOXC1
TWIST2
HES7
MSX1
WNT6
CDX2
GO: pattern specification process
GO: sensory organ development
Cluster 4
TBX6
SP5
SOX17
EVX1
MESP1
WNT3A
TBXT
GO: regionalization
Cluster 5
SYCP1
WT1
PIWIL1
LHX1
GO: synaptonemal complex assembly
GO: developmental process involved in reproduction
z−score(FPKM)
membership
C
Ectoderm
D
Mesoderm
E
Endoderm
−log10(P.value)
Enrich_ratio
Common
Mouse
Monkey
F
Species
Mouse
Monkey
Human
Enrich Score
G
Anova, p = 0.034
FOXO6 activity
M.fas
Mus
Hum
H
I
J
Positive
Negative
Low
High

1213 **Figure S8 Cross-species spatial transcriptomic analysis reveals**
1214 **gastrulation developmental differences among mice, monkeys and**
1215 **humans**

1216 A, Heatmap of Spearman correlation coefficient of expressed gene between
1217 mouse and monkey gastrulating embryos.
1218 B, Cluster analysis of the gene expression patterns across the gastrulation
1219 development stages.
1220 C-E, Dotplot showing functional enrichment of species – specificity regulons in
1221 ectoderm (C), mesoderm (D) and endoderm (E) formation between mouse and
1222 macaque.
1223 F, Functional enrichment, interactome analysis and gene annotation based on
1224 species – specificity regulons.
1225 G, The activities of FOXO6 regulons between mouse, monkey and human
1226 gastrulation embryonic tissue.
1227 H-J, Networks showing the relationship of FOXO1 (H), FOXO3 (I) and FOXO4
1228 (J) with their targets and top 10 related genes, respectively. The color of edges
1229 means positive interaction (orange) or negative interaction (green), and the
1230 width of edges represents the strength of the correlation.
1231
1232

1233 **Table S1. List of the length and thickness of sectioned epiblast from E17**
1234 **to E20, Related to Figure 1**

1235 The gastrulating embryo sizes were assessed by the length and thickness of
1236 sectioned epiblast.

1237 **Table S2. Cell counting of germ layers in gastrulating Cynomolgus**
1238 **monkey embryos, Related to Figure 1**

1239 The detailed histological analysis was applied to determine cell number by
1240 counting nuclei on every section of the gastrulating embryos. The total score
1241 was then adjusted by applying Abercrombie's correction formula to give an
1242 estimate of the actual cell number.

1243 **Table S3. The interspecies differences underlying the germ layer**
1244 **segregation, Related to Figure 7**

1245 The species/spatial domain- specificity score (SSS) of mouse and macaque in
1246 the process of ectoderm, mesoderm and endoderm specification was showed
1247 in sheet 1. The SSS and p-value of interspecies differences in mouse, macaque
1248 and human were listed in sheet 2. The species-specific regulons were listed in
1249 sheet 3.
1250
1251
1252

REFERENCE

Abe, T., Sakaue-Sawano, A., Kiyonari, H., Shioi, G., Inoue, K., Horiuchi, T., Nakao, K., Miyawaki, A., Aizawa, S., and Fujimori, T. (2013). Visualization of cell cycle in mouse embryos with Fucci2 reporter directed by Rosa26 promoter. Development *140*, 237-246.

Abercrombie, M. (1946). Estimation of nuclear population from microtome sections. The Anatomical record *94*, 239-247.

Aibar, S., Gonzalez-Blas, C.B., Moerman, T., Huynh-Thu, V.A., Imrichova, H., Hulselmans, G., Rambow, F., Marine, J.C., Geurts, P., Aerts, J.*, et al.* (2017). SCENIC: single-cell regulatory network inference and clustering. Nature methods.

Andreatta, M., and Carmona, S.J. (2021). UCell: Robust and scalable single-cell gene signature scoring. Computational and structural biotechnology journal *19*, 3796-3798.

Baardman, M.E., Kerstjens-Frederikse, W.S., Berger, R.M., Bakker, M.K., Hofstra, R.M., and Plösch, T. (2013). The role of maternal-fetal cholesterol transport in early fetal life: current insights. Biology of reproduction *88*, 24.

Ben-Haim, N., Lu, C., Guzman-Ayala, M., Pescatore, L., Mesnard, D., Bischofberger, M., Naef, F., Robertson, E.J., and Constam, D.B. (2006). The nodal precursor acting via activin receptors induces mesoderm by maintaining a source of its convertases and BMP4. Developmental cell *11*, 313-323.

Bianchi, D.W., Wilkins-Haug, L.E., Enders, A.C., and Hay, E.D. (1993). Origin of extraembryonic mesoderm in experimental animals: relevance to chorionic mosaicism in humans. American journal of medical genetics *46*, 542-550.

Boroviak, T., Stirparo, G.G., Dietmann, S., Hernando-Herraez, I., Mohammed, H., Reik, W., Smith, A., Sasaki, E., Nichols, J., and Bertone, P. (2018). Single cell transcriptome analysis of human, marmoset and mouse embryos reveals common and divergent features of preimplantation development. Development *145*.

Brennan, J., Lu, C.C., Norris, D.P., Rodriguez, T.A., Beddington, R.S., and Robertson, E.J. (2001). Nodal signalling in the epiblast patterns the early mouse embryo. Nature *411*, 965-969.

Bu, D., Luo, H., Huo, P., Wang, Z., Zhang, S., He, Z., Wu, Y., Zhao, L., Liu, J., Guo, J.*, et al.* (2021). KOBAS-i: intelligent prioritization and exploratory visualization of biological functions for gene enrichment analysis. Nucleic acids research *49*, W317-W325.

Carlson, B.M. (2015). Gastrulation and Germ Layer Formation. In Reference Module in Biomedical Sciences.

Chakraborty, P., George, J.T., Tripathi, S., Levine, H., and Jolly, M.K. (2020). Comparative Study of Transcriptomics-Based Scoring Metrics for the Epithelial-

Hybrid-Mesenchymal Spectrum. Front Bioeng Biotechnol *8*, 220.
Chakravarti, D., LaBella, K.A., and DePinho, R.A. (2021). Telomeres: history, health, and hallmarks of aging. Cell *184*, 306-322.
Chen, J., Suo, S., Tam, P.P., Han, J.J., Peng, G., and Jing, N. (2017). Spatial transcriptomic analysis of cryosectioned tissue samples with Geo-seq. Nature protocols *12*, 566-580.
Chen, S., Zhou, Y., Chen, Y., and Gu, J. (2018). fastp: an ultra-fast all-in-one FASTQ preprocessor. Bioinformatics *34*, i884-i890.
Chhabra, S., Liu, L., Goh, R., Kong, X., and Warmflash, A. (2019). Dissecting the dynamics of signaling events in the BMP, WNT, and NODAL cascade during self-organized fate patterning in human gastruloids. PLoS biology *17*, e3000498.
Cindrova-Davies, T., Jauniaux, E., Elliot, M.G., Gong, S., Burton, G.J., and Charnock-Jones, D.S. (2017). RNA-seq reveals conservation of function among the yolk sacs of human, mouse, and chicken. Proceedings of the National Academy of Sciences of the United States of America *114*, E4753-E4761.
Ciruna, B., and Rossant, J. (2001). FGF Signaling Regulates Mesoderm Cell Fate Specification and Morphogenetic Movement at the Primitive Streak. Developmental cell *1*, 37-49.
Cui, G., Chen, J., Chen, S., Qian, Y., Peng, G., and Jing, N. (2019). Spatio-temporal transcriptome construction of early mouse embryo with Geo-seq and Auto-seq. Protocol Exchange, 10.21203/rs.21202.10081/v21201.
de Bakker, B.S., de Jong, K.H., Hagoort, J., de Bree, K., Besselink, C.T., de Kanter, F.E.C., Veldhuis, T., Bais, B., Schildmeijer, R., Ruijter, J.M.*, et al.* (2016). An interactive three-dimensional digital atlas and quantitative database of human development. Science *354*, aag0053.
DeTomaso, D., Jones, M.G., Subramaniam, M., Ashuach, T., Ye, C.J., and Yosef, N. (2019). Functional interpretation of single cell similarity maps. Nature communications *10*, 4376.
Dong, D., and Yang, P. (2018). Yolk Sac. In Encyclopedia of Reproduction (Second Edition), M.K. Skinner, ed. (Oxford: Academic Press), pp. 551-558.
Dongre, A., and Weinberg, R.A. (2019). New insights into the mechanisms of epithelial-mesenchymal transition and implications for cancer. Nature reviews Molecular cell biology *20*, 69-84.
Drost, H.-G. (2018). Philentropy: Information Theory and Distance Quantification with R. Journal of Open Source Software *3*.
Dufort, D., Schwartz, L., Harpal, K., and Rossant, J. (1998). The transcription factor HNF3beta is required in visceral endoderm for normal primitive streak morphogenesis. Development *125*, 3015-3025.
Eivers, E., McCarthy, K., Glynn, C., Nolan, C.M., and Byrnes, L. (2004). Insulin-like growth factor (IGF) signalling is required for early dorso-anterior

development of the zebrafish embryo. The International journal of developmental biology *48*, 1131-1140.
Elosua-Bayes, M., Nieto, P., Mereu, E., Gut, I., and Heyn, H. (2021). SPOTlight: seeded NMF regression to deconvolute spatial transcriptomics spots with single-cell transcriptomes. Nucleic acids research.
Enders, A.C., and King, B.F. (1988). Formation and differentiation of extraembryonic mesoderm in the rhesus monkey. The American journal of anatomy *181*, 327-340.
Enders, A.C., Schlafke, S., and Hendrickx, A.G. (1986). Differentiation of the embryonic disc, amnion, and yolk sac in the rhesus monkey. The American journal of anatomy *177*, 161-185.
Exalto, N. (1995). Early human nutrition. European Journal of Obstetrics & Gynecology and Reproductive Biology *61*, 3-6.
Feng, S., Xing, C., Shen, T., Qiao, Y., Wang, R., Chen, J., Liao, J., Lu, Z., Yang, X., Abd-Allah, S.M.*, et al.* (2017). Abnormal Paraventricular Nucleus of Hypothalamus and Growth Retardation Associated with Loss of Nuclear Receptor Gene COUP-TFII. Scientific reports *7*, 5282.
Fu, J., Warmflash, A., and Lutolf, M.P. (2020). Stem-cell-based embryo models for fundamental research and translation. Nature materials.
Gao, Y., Cao, Q., Lu, L., Zhang, X., Zhang, Z., Dong, X., Jia, W., and Cao, Y. (2015). Kruppel-like factor family genes are expressed during Xenopus embryogenesis and involved in germ layer formation and body axis patterning. *244*, 1328-1346.
Ghimire, S., Mantziou, V., Moris, N., and Arias, A.M. (2021). Human gastrulation: The embryo and its models. Developmental biology.
Grapin-Botton, A., and Constam, D. (2007). Evolution of the mechanisms and molecular control of endoderm formation. Mechanisms of development *124*, 253-278.
Grobstein, C. (1985). The early development of human embryos. The Journal of medicine and philosophy *10*, 213-236.
Gualdi, R., Bossard, P., Zheng, M., Hamada, Y., Coleman, J.R., and Zaret, K.S. (1996). Hepatic specification of the gut endoderm in vitro: cell signaling and transcriptional control. Genes & development *10*, 1670-1682.
Hannenhalli, S., and Kaestner, K.H. (2009). The evolution of Fox genes and their role in development and disease. Nature reviews Genetics *10*, 233-240.
Hendrickx, A.G. (1972). Early development of the embryo in non-human primates and man. Acta endocrinologica Supplementum *166*, 103-130.
Hyun, I., Bredenoord, A.L., Briscoe, J., Klipstein, S., and Tan, T. (2021). Human embryo research beyond the primitive streak. Science *371*, 998-1000.
Jin, S., Guerrero-Juarez, C.F., Zhang, L., Chang, I., Ramos, R., Kuan, C.H., Myung, P., Plikus, M.V., and Nie, Q. (2021). Inference and analysis of cell-cell communication using CellChat. Nature communications *12*, 1088.

Kaestner, K.H., Hiemisch, H., and Schütz, G. (1998). Targeted disruption of the gene encoding hepatocyte nuclear factor 3gamma results in reduced transcription of hepatocyte-specific genes. Molecular and cellular biology *18*, 4245-4251.

Lai, E., Prezioso, V.R., Tao, W.F., Chen, W.S., and Darnell, J.E., Jr. (1991). Hepatocyte nuclear factor 3 alpha belongs to a gene family in mammals that is homologous to the Drosophila homeotic gene fork head. Genes & development *5*, 416-427.

Lamouille, S., Xu, J., and Derynck, R. (2014). Molecular mechanisms of epithelial-mesenchymal transition. Nature reviews Molecular cell biology *15*, 178-196.

Langfelder, P., and Horvath, S. (2008). WGCNA: an R package for weighted correlation network analysis. BMC bioinformatics *9*, 559.

Larsson, L., Frisen, J., and Lundeberg, J. (2021). Spatially resolved transcriptomics adds a new dimension to genomics. Nature methods *18*, 15-18.

Lawson, K.A., and Wilson, V. (2016). A Revised Staging of Mouse Development Before Organogenesis. In Kaufman's Atlas of Mouse Development Supplement, pp. 51-64.

Luckett, W.P. (1978). Origin and differentiation of the yolk sac and extraembryonic mesoderm in presomite human and rhesus monkey embryos. The American journal of anatomy *152*, 59-97.

Ma, H., Zhai, J., Wan, H., Jiang, X., Wang, X., Wang, L., Xiang, Y., He, X., Zhao, Z.A., Zhao, B.*, et al.* (2019). In vitro culture of Cynomolgus monkey embryos beyond early gastrulation. Science *366*.

Massri, A.J., Schiebinger, G.R., Berrio, A., Wang, L., Wray, G.A., and McClay, D.R. (2021). The Epithelialto Mesenchymal Transition. Methods Mol Biol *2179*, 303-314.

McDole, K., Guignard, L., Amat, F., Berger, A., Malandain, G., Royer, L.A., Turaga, S.C., Branson, K., and Keller, P.J. (2018). In Toto Imaging and Reconstruction of Post-Implantation Mouse Development at the Single-Cell Level. Cell.

Mengjun, L.G. (2019). TCseq: Time course sequencing data analysis.

Mitiku, N., and Baker, J.C. (2007). Genomic analysis of gastrulation and organogenesis in the mouse. Developmental cell *13*, 897-907.

Mittnenzweig, M., Mayshar, Y., Cheng, S., Ben-Yair, R., Hadas, R., Rais, Y., Chomsky, E., Reines, N., Uzonyi, A., Lumerman, L.*, et al.* (2021). A single-embryo, single-cell time-resolved model for mouse gastrulation. Cell.

Monaghan, A.P., Kaestner, K.H., Grau, E., and Schütz, G. (1993). Postimplantation expression patterns indicate a role for the mouse forkhead/HNF-3 alpha, beta and gamma genes in determination of the definitive endoderm, chordamesoderm and neuroectoderm. Development *119*, 567-578.

Moore, H.D., Gems, S., and Hearn, J.P. (1985). Early implantation stages in the

marmoset monkey (Callithrix jacchus). The American journal of anatomy *172*, 265-278.
Moris, N., Anlas, K., van den Brink, S.C., Alemany, A., Schröder, J., Ghimire, S., Balayo, T., van Oudenaarden, A., and Martinez Arias, A. (2020). An in vitro model of early anteroposterior organization during human development. Nature *582*, 410-415.
Muller, F., and O'Rahilly, R. (2004). The primitive streak, the caudal eminence and related structures in staged human embryos. Cells, tissues, organs *177*, 2-20.
Nakamura, T., Fujiwara, K., Saitou, M., and Tsukiyama, T. (2021). Non-human primates as a model for human development. Stem Cell Reports *16*, 1093-1103.
Nakamura, T., Okamoto, I., Sasaki, K., Yabuta, Y., Iwatani, C., Tsuchiya, H., Seita, Y., Nakamura, S., Yamamoto, T., and Saitou, M. (2016). A developmental coordinate of pluripotency among mice, monkeys and humans. Nature *537*, 57-62.
Nicetto, D., Donahue, G., Jain, T., Peng, T., Sidoli, S., Sheng, L., Montavon, T., Becker, J.S., Grindheim, J.M., Blahnik, K.*, et al.* (2019). H3K9me3-heterochromatin loss at protein-coding genes enables developmental lineage specification. *363*, 294-297.
Nikolopoulou, E., Galea, G.L., Rolo, A., Greene, N.D., and Copp, A.J. (2017). Neural tube closure: cellular, molecular and biomechanical mechanisms. Development *144*, 552-566.
Niu, Y., Sun, N., Li, C., Lei, Y., Huang, Z., Wu, J., Si, C., Dai, X., Liu, C., Wei, J.*, et al.* (2019). Dissecting primate early post-implantation development using long-term in vitro embryo culture. Science *366*, 5754.
Nowotschin, S., Hadjantonakis, A.K., and Campbell, K. (2019). The endoderm: a divergent cell lineage with many commonalities. Development *146*, dev150920.
O'Rahilly, R., and Muller, F. (2010). Developmental stages in human embryos: revised and new measurements. Cells, tissues, organs *192*, 73-84.
Otasek, D., Morris, J.H., Boucas, J., Pico, A.R., and Demchak, B. (2019). Cytoscape Automation: empowering workflow-based network analysis. Genome biology *20*, 185.
Peng, G., Cui, G., Ke, J., and Jing, N. (2020a). Using Single-Cell and Spatial Transcriptomes to Understand Stem Cell Lineage Specification During Early Embryo Development. Annual Review of Genomics and Human Genetics *21*, 163-181.
Peng, G., Cui, G., Ke, J., and Jing, N. (2020b). Using Single-Cell and Spatial Transcriptomes to Understand Stem Cell Lineage Specification During Early Embryo Development. Annu Rev Genomics Hum Genet *21*, 163-181.
Peng, G., Suo, S., Chen, J., Chen, W., Liu, C., Yu, F., Wang, R., Chen, S., Sun, N., Cui, G.*, et al.* (2016). Spatial Transcriptome for the Molecular Annotation of

Lineage Fates and Cell Identity in Mid-gastrula Mouse Embryo. Developmental cell *36*, 681-697.
Peng, G., Suo, S., Cui, G., Yu, F., Wang, R., Chen, J., Chen, S., Liu, Z., Chen, G., Qian, Y.*, et al.* (2019). Molecular architecture of lineage allocation and tissue organization in early mouse embryo. Nature *572*, 528-532.
Peng, H., Ruan, Z., Long, F., Simpson, J.H., and Myers, E.W. (2010). V3D enables real-time 3D visualization and quantitative analysis of large-scale biological image data sets. Nat Biotechnol *28*, 348-353.
Pertea, M., Kim, D., Pertea, G.M., Leek, J.T., and Salzberg, S.L. (2016). Transcript-level expression analysis of RNA-seq experiments with HISAT, StringTie and Ballgown. Nature protocols *11*, 1650-1667.
Pfister, S., Steiner, K.A., and Tam, P.P. (2007). Gene expression pattern and progression of embryogenesis in the immediate post-implantation period of mouse development. Gene expression patterns : GEP *7*, 558-573.
Pijuan-Sala, B., Guibentif, C., and Gottgens, B. (2018). Single-cell transcriptional profiling: a window into embryonic cell-type specification. Nature reviews Molecular cell biology.
Rivera-Perez, J.A., and Hadjantonakis, A.K. (2015). The Dynamics of Morphogenesis in the Early Mouse Embryo. Cold Spring Harb Perspect Biol *7*.
Rivera-Perez, J.A., and Magnuson, T. (2005). Primitive streak formation in mice is preceded by localized activation of Brachyury and Wnt3. Developmental biology *288*, 363-371.
Ross, C., and Boroviak, T.E. (2020). Origin and function of the yolk sac in primate embryogenesis. Nature communications *11*, 3760.
Sasaki, H., and Hogan, B.L. (1993). Differential expression of multiple fork head related genes during gastrulation and axial pattern formation in the mouse embryo. Development *118*, 47-59.
Scheibner, K., Schirge, S., Burtscher, I., Buttner, M., Sterr, M., Yang, D., Bottcher, A., Ansarullah, Irmler, M., Beckers, J.*, et al.* (2021). Epithelial cell plasticity drives endoderm formation during gastrulation. Nat Cell Biol.
Schindelin, J., Arganda-Carreras, I., Frise, E., Kaynig, V., Longair, M., Pietzsch, T., Preibisch, S., Rueden, C., Saalfeld, S., Schmid, B.*, et al.* (2012). Fiji: an open-source platform for biological-image analysis. Nature methods *9*, 676-682.
Shahbazi, M.N. (2020). Mechanisms of human embryo development: from cell fate to tissue shape and back. Development *147*, dev190629.
Sheaffer, K.L., and Kaestner, K.H. (2012). Transcriptional networks in liver and intestinal development. Cold Spring Harb Perspect Biol *4*, a008284.
Singh, M., Yelle, N., Venugopal, C., and Singh, S.K. (2018). EMT: Mechanisms and therapeutic implications. Pharmacol Ther *182*, 80-94.
Snow, M. (1977). Gastrulation in the mouse: growth and regionalization of the epiblast. Journal of embryology and experimental morphology *42*, 293-303.
Souilhol, C., Perea-Gomez, A., Camus, A., Beck-Cormier, S., Vandormael-

1503 Pournin, S., Escande, M., Collignon, J., and Cohen-Tannoudji, M. (2015).
1504 NOTCH activation interferes with cell fate specification in the gastrulating
1505 mouse embryo. Development *142*, 3649-3660.
1506 Stuart, T., Butler, A., Hoffman, P., Hafemeister, C., Papalexi, E., Mauck, W.M.,
1507 3rd, Hao, Y., Stoeckius, M., Smibert, P., and Satija, R. (2019). Comprehensive
1508 Integration of Single-Cell Data. Cell *177*, 1888-1902 e1821.
1509 Sun, X., Meyers, E.N., Lewandoski, M., and Martin, G.R. (1999). Targeted
1510 disruption of Fgf8 causes failure of cell migration in the gastrulating mouse
1511 embryo. Genes & development *13*, 1834-1846.
1512 Suo, S., Zhu, Q., Saadatpour, A., Fei, L., Guo, G., and Yuan, G.C. (2018).
1513 Revealing the Critical Regulators of Cell Identity in the Mouse Cell Atlas. Cell
1514 Rep *25*, 1436-1445 e1433.
1515 Tam, P.P., and Behringer, R.R. (1997). Mouse gastrulation: the formation of a
1516 mammalian body plan. Mechanisms of development *68*, 3-25.
1517 Tam, P.P.L., and Ho, J.W.K. (2020). Cellular diversity and lineage trajectory:
1518 insights from mouse single cell transcriptomes. Development *147*.
1519 Tang, T.T.-L., Dowbenko, D., Jackson, A., Toney, L., Lewin, D.A., Dent, A.L., and
1520 Lasky, L.A. (2002). The Forkhead Transcription Factor AFX Activates Apoptosis
1521 by Induction of the BCL-6 Transcriptional Repressor *. Journal of Biological
1522 Chemistry *277*, 14255-14265.
1523 Tani, S., Chung, U.I., Ohba, S., and Hojo, H. (2020). Understanding paraxial
1524 mesoderm development and sclerotome specification for skeletal repair. Exp
1525 Mol Med.
1526 Tarara, R., Enders, A.C., Hendrickx, A.G., Gulamhusein, N., Hodges, J.K.,
1527 Hearn, J.P., Eley, R.B., and Else, J.G. (1987). Early implantation and embryonic
1528 development of the baboon: stages 5, 6 and 7. Anat Embryol (Berl) *176*, 267-
1529 275.
1530 Thieme, R., Ramin, N., Fischer, S., Puschel, B., Fischer, B., and Santos, A.N.
1531 (2012). Gastrulation in rabbit blastocysts depends on insulin and insulin-like-
1532 growth-factor 1. Molecular and cellular endocrinology *348*, 112-119.
1533 Tyser, R.C.V., Mahammadov, E., Nakanoh, S., Vallier, L., Scialdone, A., and
1534 Srinivas, S. (2020). A spatially resolved single cell atlas of human gastrulation.
1535 Tyser, R.C.V., Mahammadov, E., Nakanoh, S., Vallier, L., Scialdone, A., and
1536 Srinivas, S. (2021). Single-cell transcriptomic characterization of a gastrulating
1537 human embryo. Nature.
1538 Varelas, X., Sakuma, R., Samavarchi-Tehrani, P., Peerani, R., Rao, B.M.,
1539 Dembowy, J., Yaffe, M.B., Zandstra, P.W., and Wrana, J.L. (2008). TAZ controls
1540 Smad nucleocytoplasmic shuttling and regulates human embryonic stem-cell
1541 self-renewal. Nat Cell Biol *10*, 837-848.
1542 Viotti, M., Nowotschin, S., and Hadjantonakis, A.K. (2014). SOX17 links gut
1543 endoderm morphogenesis and germ layer segregation. Nat Cell Biol *16*, 1146-
1544 1156.

Wang, C., Liu, X., Gao, Y., Yang, L., Li, C., Liu, W., Chen, C., Kou, X., Zhao, Y., Chen, J., *et al.* (2018). Reprogramming of H3K9me3-dependent heterochromatin during mammalian embryo development. Nat Cell Biol *20*, 620-631.

Wong, E.A., and Uni, Z. (2021). Centennial Review: The chicken yolk sac is a multifunctional organ. Poult Sci *100*, 100821.

Xiang, L., Yin, Y., Zheng, Y., Ma, Y., Li, Y., Zhao, Z., Guo, J., Ai, Z., Niu, Y., Duan, K., *et al.* (2019). A developmental landscape of 3D-cultured human pre-gastrulation embryos. Nature *577*, 537-542.

Yamasaki, J., Iwatani, C., Tsuchiya, H., Okahara, J., Sankai, T., and Torii, R. (2011). Vitrification and transfer of Cynomolgus monkey (Macaca fascicularis) embryos fertilized by intracytoplasmic sperm injection. Theriogenology *76*, 33-38.

Yamashita, S., Ogawa, K., Ikei, T., Fujiki, T., and Katakura, Y. (2014). FOXO3a potentiates hTERT gene expression by activating c-MYC and extends the replicative life-span of human fibroblast. PloS one *9*, e101864.

Yang, J., Wang, B., Chen, H., Chen, X., Li, J., Chen, Y., Yuan, D., and Zheng, S. (2019). Thyrotroph embryonic factor is downregulated in bladder cancer and suppresses proliferation and tumorigenesis via the AKT/FOXOs signalling pathway. Cell Prolif *52*, e12560.

Yang, R., Goedel, A., Kang, Y., Si, C., Chu, C., Zheng, Y., Chen, Z., Gruber, P.J., Xiao, Y., Zhou, C., *et al.* (2021). Amnion signals are essential for mesoderm formation in primates. Nature communications *12*, 5126.

Yeung, T.L., Leung, C.S., Wong, K.K., Gutierrez-Hartmann, A., Kwong, J., Gershenson, D.M., and Mok, S.C. (2017). ELF3 is a negative regulator of epithelial-mesenchymal transition in ovarian cancer cells. Oncotarget *8*, 16951-16963.

Yu, G., Wang, L.G., Han, Y., and He, Q.Y. (2012). clusterProfiler: an R package for comparing biological themes among gene clusters. OMICS *16*, 284-287.

Zhang, X., Yalcin, S., Lee, D.F., Yeh, T.Y., Lee, S.M., Su, J., Mungamuri, S.K., Rimmele, P., Kennedy, M., Sellers, R., *et al.* (2011). FOXO1 is an essential regulator of pluripotency in human embryonic stem cells. Nat Cell Biol *13*, 1092-1099.

Zhang, Y., Ma, Y., Huang, Y., Zhang, Y., Jiang, Q., Zhou, M., and Su, J. (2020). Benchmarking algorithms for pathway activity transformation of single-cell RNA-seq data. Computational and structural biotechnology journal *18*, 2953-2961.

Zheng, Y., Xue, X., Shao, Y., Wang, S., Esfahani, S.N., Li, Z., Muncie, J.M., Lakins, J.N., Weaver, V.M., Gumucio, D.L., *et al.* (2019). Controlled modelling of human epiblast and amnion development using stem cells. Nature *573*, 421-425.

Zhou, Y., Zhou, B., Pache, L., Chang, M., Khodabakhshi, A.H., Tanaseichuk, O.,

Benner, C., and Chanda, S.K. (2019). Metascape provides a biologist-oriented resource for the analysis of systems-level datasets. Nature communications *10*, 1523.